EXPERIMENTAL INVESTIGATION OF THE HELICOPTER BLADE TIP SHAPE EFFECTS ON AERODYNAMIC PERFORMANCE AND TIP VORTEX CHARACTERISTICS

A THESIS SUBMITTED TO
THE GRADUATE SCHOOL OF NATURAL AND APPLIED SCIENCES
OF
MIDDLE EAST TECHNICAL UNIVERSITY

BY

SİNEM ULUOCAK

IN PARTIAL FULFILLMENT OF THE REQUIREMENTS
FOR
THE DEGREE OF MASTER OF SCIENCE
IN
AEROSPACE ENGINEERING

JANUARY 2019

Approval of the thesis:

EXPERIMENTAL INVESTIGATION OF THE HELICOPTER BLADE TIP SHAPE EFFECTS ON AERODYNAMIC PERFORMANCE AND TIP VORTEX CHARACTERISTICS

submitted by **SİNEM ULUOCAK** in partial fulfillment of the requirements for the degree of **Master of Science in Aerospace Engineering Department, Middle East Technical University** by,

Prof. Dr. Halil Kalıpçılar
Dean, Graduate School of **Natural and Applied Sciences** _______________

Prof. Dr. İsmail H. Tuncer
Head of Department, **Aerospace Engineering** _______________

Assist. Prof. Dr. Mustafa Perçin
Supervisor, **Aerospace Engineering, METU** _______________

Prof. Dr. Oğuz Uzol
Co-supervisor, **Aerospace Engineering, METU** _______________

Examining Committee Members:

Prof. Dr. Yusuf Özyörük
Aerospace Engineering, METU _______________

Assist. Prof. Dr. Mustafa Perçin
Aerospace Engineering Department, METU _______________

Prof. Dr. Oğuz Uzol
Aerospace Engineering, METU _______________

Assoc. Prof. Dr. Utku Kanoğlu
Aerospace Engineering, METU _______________

Assist. Prof. Dr. Onur Baş
Mechanical Engineering, TED University _______________

Date: 28.01.2019

I hereby declare that all information in this document has been obtained and presented in accordance with academic rules and ethical conduct. I also declare that, as required by these rules and conduct, I have fully cited and referenced all material and results that are not original to this work.

Name, Surname: Sinem Uluocak

Signature :

ABSTRACT

EXPERIMENTAL INVESTIGATION OF THE HELICOPTER BLADE TIP SHAPE EFFECTS ON AERODYNAMIC PERFORMANCE AND TIP VORTEX CHARACTERISTICS

Uluocak, Sinem
M.S., Department of Aerospace Engineering
Supervisor: Assist. Prof. Dr. Mustafa Perçin
Co-Supervisor : Prof. Dr. Oğuz Uzol

January 2019, 79 pages

This study experimentally investigates the effects of different rotor blade tip shapes on the rotor aerodynamic performance and the tip vortex characteristics in hovering flight. Force, torque and flow field measurements were performed on a 1.3 m diameter 5-bladed model rotor for four different blades: rectangular (RECT), anhedral (ANHD), tapered-swept (TAPER) and tapered-swept-anhedral (TSA). Thrust and torque measurements show that all tip modifications have a positive effect on the aerodynamic performance when compared to the RECT tip configuration especially at low blade loadings. Overall, the ANHD tip configuration gives the best aerodynamic performance at high blade loadings. It reaches a maximum figure of merit (FOM) value of 0.67 and provides a FOM improvement of approximately 0.03 compared to the RECT blade at the tip Mach number (M_{tip}) of 0.3. Phase-locked particle image velocimetry measurements were conducted at 6° intervals between 0° -72° phase/wake ages at the selected pitch angle of 16° and $M_{tip} = 0.4$. It is observed that tip modifications change the tip vortex trajectory by increasing radial convection speed and decreasing axial convection speed. ANHD reduces the maximum vortex

tangential velocity up to 20%; the TAPER and the TSA reduces it up to 30%. The minimum tip-vortex circulation level is achieved in the case of the ANHD blade, which is in agreement with the highest FOM obtained with this blade.

Keywords: Rotor aerodynamic performance, hovering flight, tip vortex, rotor tip modifications, particle image velocimetry

ÖZ

HELİKOPTER PAL UCU ŞEKLİNİN AERODİNAMİK PERFORMANS VE UÇ GİRDABI KARAKTERİSTİĞİ ÜZERİNE ETKİLERİNİN DENEYSEL OLARAK İNCELENMESİ

Uluocak, Sinem
Yüksek Lisans, Havacılık ve Uzay Bölümü
Tez Yöneticisi: Dr. Öğr. Üyesi. Mustafa Perçin
Ortak Tez Yöneticisi : Prof. Dr. Oğuz Uzol

Ocak 2019 , 79 sayfa

Bu çalışma, farklı rotor pal ucu şekillerinin rotor aerodinamik performansına ve uç girdabı karakteristiğine etkisini askı uçuşu durumunda deneysel olarak incelemektedir. Kuvvet, tork ve akış alanı ölçümleri 1.3 m çapa sahip 5 palli bir model rotor kullanılarak, düz (RECT), anhedral (ANHD), tapered-swept (TAPER) ve tapered-swept-anhedral (TSA) olmak üzere 4 farklı pal için yapılmıştır. İtki ve tork ölçümleri, modifikasyona uğramış pallerin özellikle düşük pal yüklemelerinde aerodinamik performansa pozitif bir etkisi olduğunu göstermektedir. Toplamda ise, ANHD konfigurasyonunun yüksek pal yüklemelerinde ve uç Mach sayısı 0.3 iken en iyi aerodinamik performansı gösterdiği, maksimum 0.67 FOM değerine ulaşarak RECT pale göre 0.03 FOM artışı sağladığı bulunmuştur. Faz kilitlemeli parçacık görüntülemeli hız ölçme tekniği kullanılarak yapılan akış ölçümleri 6° aralıklarla 0° -72° faz açıları arasında 16° pitch açısı için uç Mach sayısı 0.4'te yürütülmüştür. Uç modifikasyonlarının radyal taşıma hızını artırıp, eksenel taşıma hızını azaltarak girdap yörüngesini değiştirdiği gözlemlenmiştir. ANHD pal maksimum girdap hızını %20'ye, TAPER ve

TSA paller %30'a kadar azaltmıştır. Minimum girdaplılık değeri aynı zamanda en iyi FOM değerini veren ANHD pal geometrisi kullanıldığında elde edilmiştir.

Anahtar Kelimeler: Rotor aerodinamik performans, askı uçuş, uç girdap, rotor pal modifikasyonu, parçacık görüntülemeli hız ölçme tekniği

Dedicated to Mustafa Kemal Atatürk for his trust in Turkish youth

ACKNOWLEDGMENTS

First of all, I would like to thank to my co-advisor Prof. Dr. Oğuz Uzol for introducing me to the experimental aerodynamics and this project. I am grateful to him for his knowledge and guidance for all the time.

I would also like to extend my deepest gratitude to my supervisor Assist. Prof. Dr. Mustafa Perçin for his knowledge, motivation, kindness and support throughout the study.

I also has great pleasure of working with Hooman Amiri Hazaveh, Tuğrul Akpolat, Enes Coşkun, Yashar Ostovan and Onur Gençoğlu in this study, I wish to thank to them for the time full of brainstorming, experiments and fun.

I also would like to thank Hakan İşçi and Murat Ceyhan for supporting this thesis and giving me the chance to work for this intriguing research and development project as a part of the Rotary Wing Technology Center. I am grateful to meet here with the best colleagues and friends Cansu Karataş, Senem Aktaş, Ali Oğuz Yüksel, Mehmet Ali Yavuz, Ali Kıvanç Ersan, Gökçe Özgül and Ozan Alican for the enjoyful times that we spent together.

I would like to express my eternal gratitude to my family, my lovely sister Seray Hisarkaya and my best friend Özge Beğli for their support throughout my life. Lastly, I am grateful for having the friendship and love of Erdem Dinçer.

This study is funded by Turkish Aerospace as a part of the project DKTM/2015/13.

TABLE OF CONTENTS

ABSTRACT . . . v

ÖZ . . . vii

ACKNOWLEDGMENTS . . . x

TABLE OF CONTENTS . . . xi

LIST OF TABLES . . . xiv

LIST OF FIGURES . . . xv

LIST OF ABBREVIATIONS . . . xviii

CHAPTERS

1 INTRODUCTION . . . 1

1.1 Overview on Helicopter Aerodynamics and Performance . . . 1

1.1.1 Hovering Flight . . . 1

1.1.2 Forward Flight . . . 7

1.2 Tip Vortex Phenomenon and Characteristics . . . 9

1.3 Literature Survey on Different Tip Shapes . . . 14

1.4 Objective and Scope of the Thesis . . . 18

2 EXPERIMENTAL SETUP AND METHODOLOGY . . . 21

2.1 Background About Rotor Test Stands . . . 21

2.2 The Design of the Experimental Setup . . . 25

2.2.1 Preliminary Design 25

2.2.2 Selection of the Sensors 27

2.2.3 CFD Analysis of the Setup 28

2.3 Design of the Rotor 29

2.3.1 Structural Analysis of the Rotor 30

2.3.2 Tip Modifications 32

2.4 Final design of the Setup 33

2.5 Characterization of the System 36

2.5.1 Alignment and Vibration Analyses 36

2.5.2 Calibration of Thrust Measurements 39

2.6 Measurement Details 39

2.6.1 Thrust and Torque Measurements 40

2.6.2 Flow Field Measurements via PIV 40

2.6.3 Post-Processing Methods 43

2.7 Analysis of Measurement Errors 45

2.7.1 Accuracy of the Thrust and Torque Measurements 45

2.7.2 Accuracy of the PIV Measurements 45

2.7.2.1 PIV measurement accuracy 45

2.7.2.2 Uncertainty in velocity vectors 46

2.7.2.3 Other sources of error for presented values 48

3 RESULTS AND DISCUSSION 49

3.1 Load Measurement Results 49

3.1.1 Comparison with BEMT 49

3.1.2 Aerodynamic Performance Graphs 52
3.2 Vortex Characteristics 57
4 CONCLUSION 69
REFERENCES 73
APPENDICES
A MEASURED THRUST AND TORQUE DATA 79

LIST OF TABLES

TABLES

Table 1.1 Experimental Studies about Tip Vortices 12

Table 2.1 Rotor properties 30

Table 2.2 Definitions of different blades 32

Table 2.3 Test matrix of thrust and torque measurements 40

Table 2.4 PIV recording parameters 41

Table 3.1 Functions of the exponential fitting models 61

Table A.1 Thrust and torque coefficients per solidity for all blades and tip Mach numbers, PIV test case was colourized 79

LIST OF FIGURES

FIGURES

Figure 1.1 Flow model for momentum theory analysis of a rotor in hovering flight [1] 2

Figure 1.2 Typical FM graph with measured data and predictions [1] 6

Figure 1.3 Flow field on rotor in hover (left) and forward flight (right) [1] . 7

Figure 1.4 Complex aerodynamics of the forward flight [1] 9

Figure 1.5 Demostration of the vortex core and tangential velocity profile [1] 10

Figure 1.6 Different tip shapes [2] 15

Figure 1.7 EC155 with the Eurocopter Blue-Edge^{TM} blade [3] 16

Figure 1.8 Westland Lynx with BERP blade [3] 16

Figure 2.1 Different rotor test setups from the literature 23

Figure 2.2 Preliminary design of the setup 26

Figure 2.3 Performance analyses 27

Figure 2.4 Instrumentation 27

Figure 2.5 Thrust coefficient (C_T) vs. Torque coefficient (C_Q) 28

Figure 2.6 CFD simulations of the rotor test setup 28

Figure 2.7 Rotor design and its parts: Blades, shaft, hub base, blade holders and locked bush. The cap is not seen in this figure. 29

Figure 2.8 Stress analysis of the rotor [48] 31

Figure 2.9 Drawings of the blades a) rectangular (baseline), b) anhedral, c) swept-tapered, d) swept-tapered-anhedral 32

Figure 2.10 Fabricated hub and blades a)swept-tapered-anhedral, b)swept-tapered c) anhedral, d) rectangular (baseline) 33

Figure 2.11 Final design of the setup 34

Figure 2.12 Different views of the final sketch of the setup 34

Figure 2.13 The setup 35

Figure 2.14 Vibration limits for rotary machines 37

Figure 2.15 Instantaneous acceleration data during the operation of 0-2000 RPM 38

Figure 2.16 FFT analysis of accelerometer data at 2000 RPM 38

Figure 2.17 Calibration of the force measurement system 39

Figure 2.18 PIV system in two different views 41

Figure 2.19 Phase angle definition 42

Figure 2.20 PIV raw image at $\phi = 0°$ 43

Figure 2.21 Post-Processing steps 44

Figure 2.22 Particle properties 46

Figure 2.23 First peak to second peak height 47

Figure 3.1 Comparison between the measurements and BEMT 51

Figure 3.2 C_T/σ vs. C_Q/σ at $M_{tip} = 0.3$ (left) and $M_{tip} = 0.4$ (right) . . . 53

Figure 3.3 C_T/σ vs. C_T/C_Q at $M_{tip} = 0.3$ (left) and $M_{tip} = 0.4$ (right) . . . 53

Figure 3.4 C$_T/\sigma$ vs. FOM at $M_{tip} = 0.3$ (left) and $M_{tip} = 0.4$ (right) 53

Figure 3.5 YUH-61A $1/5$ model (left) and full-scale tapered tip blade (right) hover performance [4] 54

Figure 3.6 Mach number vs. Cl_{max} for various airfoils including VR-7 [5] . 55

Figure 3.7 Effect of the Mach number on C_T and C_Q (for all blades) 56

Figure 3.8 Ensemble-averaged contours of out-of-plane vorticity for RECT blade 59

Figure 3.9 Vortex trajectory for all geometries 61

Figure 3.10 The overall average of 12 phases (0° to 72° with 6° intervals) for ensemble averaged vorticity (left) and ensemble averaged axial velocity (right) of each phase for all blades 62

Figure 3.11 Conditional averaged contours of out-of plane vorticity for $\phi = 42^\circ$ 63

Figure 3.12 Tangential velocity profiles at $\phi = 42^\circ$ and $\phi = 114^\circ$ 64

Figure 3.13 Maximum tangential velocities vs. Wake age 65

Figure 3.14 Tip vortex circulation vs. Wake age 66

Figure 3.15 Scatter plots for $\phi = 18^\circ$-$\phi = 138^\circ$ 67

Figure 3.16 Comparison of vortex models with measured tangential velocity data at $\phi = 42^\circ$ 68

LIST OF ABBREVIATIONS

c	Chord length
$C_{l,max}$	Maximum lift coefficient
C_T	Thrust coefficient
C_Q	Torque coefficient
M	Mach number
M_{tip}	Tip Mach number
N	Number of blades
r	Radial coordinate
r/c	Non-dimensional radial coordinate
R	Rotor radius
Re	Reynolds number
V_{tip}	Tip speed, ΩR
V_θ	Vortex tangential velocity
$V_{\theta,max}$	Vortex maximum tangential velocity
V_θ/V_{tip}	Non-dimensional vortex velocity
x	Axial coordinate
x/c	Non-dimensional axial coordinate
Γ	Circulation
Ω	Angular velocity
ϕ or Φ	Phase angle, Wake age
σ_x	Uncertainty of x
θ	Blade collective pitch angle, positive nose upward
BEMT	Blade Element Momentum Theory

BVI	Blade Vortex Interaction
CFD	Computational Fluid Dynamics
DKTM	Rotary Wing Technology Center
DLR	German Aerospace Center
FFT	Fast Fourier Transform
FM or FOM	Figure of Merit
LDV	Laser Doppler Velocimetry
PIV	Particle Image Velocimetry
TA	Turkish Aerospace

CHAPTER 1

INTRODUCTION

In this chapter, the effects of rotor tip shape on rotor aerodynamic performance and tip vortex characteristics are addressed in four sections. Firstly, helicopter aerodynamics and rotor aerodynamic performance will be briefly explained. Secondly, the phenomenon of the tip vortex and its characteristics will be summarized. Then, literature survey on different rotor tip geometries will be given. Finally, the scope of the thesis will be presented.

1.1 Overview on Helicopter Aerodynamics and Performance

Helicopter is an aircraft that uses rotating wings to provide lift, propulsion and control [6]. Different from classical aircraft, helicopters can fly vertically and preserve its condition which is known as the hovering flight, by the rotor blades producing a vertical force equal to the weight of the helicopter. In addition to the hovering flight and vertical flight (climb and descend) conditions, forward flight can be performed by tilting the rotor.

1.1.1 Hovering Flight

In the simplest form, blades create lift force due to the rotating motion supplied by an engine. The airflow is drawn through the rotor during rotation. The velocity of the air, named as induced or inflow velocity, generates kinetic energy that should be balanced to a power supply which is defined as required/ideal power. Since it is created due to the induced velocity it can be named also as induced power.

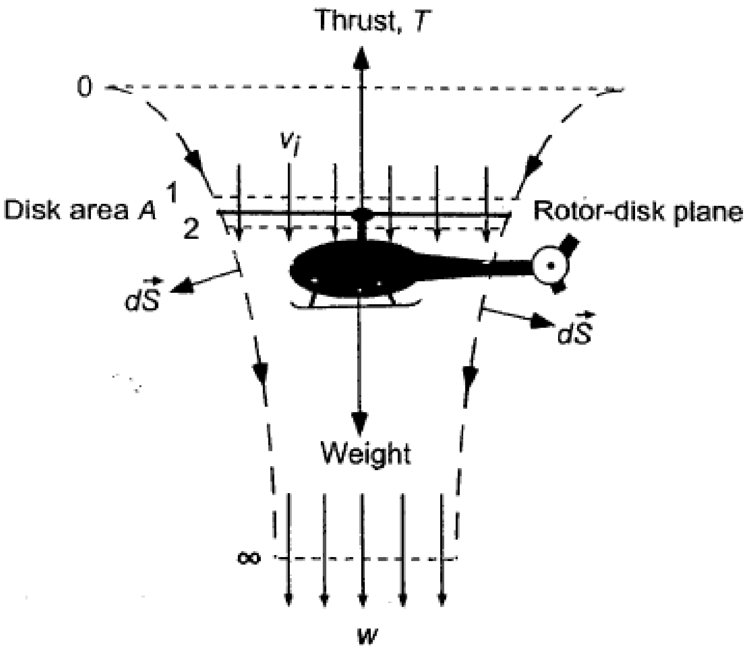

Figure 1.1: Flow model for momentum theory analysis of a rotor in hovering flight [1]

The physics of the hovering flight can be explained by using basic conservation laws with a selection of appropriate control volume and appropriate assumptions. The application of conservation laws to the hovering rotor is commonly named as "momentum theory" and will be summarised following the textbook of Leishman [1]. In this approach, rotor is accepted as an actuator disc which contains infinite number of blades with zero thickness; therefore, it does not consider the blade's aerodynamics and rotational effects. Moreover, flow through the rotor is assumed as 1-D, quasi-steady, incompressible and inviscid. The control volume and the velocities can be drawn as shown in Figure 1.1. The velocity of the fluid is zero at the upstream of the rotor which is denoted as 0. The surfaces just above and the below of the disc are denoted as 1 and 2 and the velocity of the fluid that passes through the rotor is defined as induced velocity (v_i). The far wake of the rotor is shown as ∞ and the velocity of the fluid there is denoted as w. Areas are written as A.

The conservation of the mass equation (Equation 1.1) becomes to Equation 1.2 under the assumption of 1-D incompressible flow.

$$\dot{m} = \int\int_{\infty} \rho\vec{V}.d\vec{S} = \int\int_{2} \rho\vec{V}.d\vec{S} \tag{1.1}$$

$$\dot{m} = \rho A_{\infty} w = \rho A_2 v_i \tag{1.2}$$

The momentum rate of change is equal to the applied force on the fluid and can be written for that control volume as

$$-\vec{F} = \int\int_{\infty} \rho(\vec{V}.d\vec{S})\vec{V} - \int\int_{0} \rho(\vec{V}.d\vec{S})\vec{V} \tag{1.3}$$

Since the velocity of the fluid is zero at the upstream of the rotor, it reduces to

$$-\vec{F} = \int\int_{\infty} \rho(\vec{V}.d\vec{S})\vec{V} \tag{1.4}$$

Thrust is equal and opposite to the applied force on the fluid, so it can be written as

$$T = \dot{m}w \tag{1.5}$$

The work done on the rotor is equal to the gain in energy of the fluid per unit time which is the power consumed by the rotor and can be written as Tv_i. Therefore, the equation of conservation of energy can be written as

$$P = \frac{1}{2}\int\int_{\infty} \rho(\vec{V}.d\vec{S})|\vec{V}|^2 - \frac{1}{2}\int\int_{0} \rho(\vec{V}.d\vec{S})|\vec{V}|^2 \tag{1.6}$$

Similarly, after the reduction of second term, it becomes

$$P = \frac{1}{2}\int\int_{\infty} \rho(\vec{V}.d\vec{S})|\vec{V}|^2 \tag{1.7}$$

When Tv_i is written in terms of P

$$Tv_i = \frac{1}{2}\dot{m}w^2 \tag{1.8}$$

Equation 1.5 and 1.8 result in a relation between the inflow velocity and the velocity at the far wake

$$v_i = \frac{1}{2}w \tag{1.9}$$

Since velocity and area are inversely proportional due to the conservation of mass (Equation 1.2), area at the disc and at the far wake have a relation as written below

$$A_\infty = \frac{A}{2} \tag{1.10}$$

This area reduction explains the geometric contraction of the wake but it was observed that the contraction is relatively small in the measurements which makes sense because of the non-ideal effects such as viscosity of the fluid, non-uniform inflow or rotating velocity component of the formed tip vortices.

Inserting the $2v_i$ in the place of w into the thrust and the power equation, it is seen that thrust is proportional to the square of the induced velocity and power is proportional with the cube of the induced velocity. Therefore, for a given weight or thrust of the helicopter, the induced velocity should be small for the minimum power required. Moreover, the relation between thrust and power required to hover can be written as follows

$$P = \frac{T^{3/2}}{\sqrt{2\rho A}} \tag{1.11}$$

From the above equation, it can be inferred that the larger rotor area reduces the power required for a given thrust but the diameter of the rotor is limited with size, weight, cost, tip Mach number and maneuverability requirements of the helicopter.

The non-dimensional forms of thrust and power can be written as

$$C_T = \frac{T}{\rho A(\Omega R)^2} \tag{1.12}$$

$$C_P = \frac{P}{\rho A(\Omega R)^3} \tag{1.13}$$

Then, the relation between the coefficients of thrust and power becomes

$$C_P = \frac{C_T^{3/2}}{\sqrt{2}} \tag{1.14}$$

The power in this equation is the ideal power required to hover and as mentioned earlier, it was calculated with number of assumptions and it does not contain any viscous effects. These non-ideal effects are introduced into the equation as an empirical correction factor of κ, the induced power factor, whose typical value is obtained from measurements as 1.15. So, the induced power required to hover predicted by the momentum theory can be written as

$$C_{P_i} = \frac{\kappa C_T^{3/2}}{\sqrt{2}} \tag{1.15}$$

There is always profile power comes from airfoil characteristics, therefore total power coefficient is written as the sum of the induced power coefficient (C_{d_i}) and profile power coefficient (C_{d_0})

$$C_P = C_{P_i} + C_{P_0} = \frac{\kappa C_T^{3/2}}{\sqrt{2}} + \frac{\sigma C_{d_0}}{8} \tag{1.16}$$

where, σ is solidity and C_{d_0} is profile drag coefficient.

It was previously mentioned that the efficiency of a helicopter is determined with the lowest induced power for a given weight/blade loading so that an efficiency parameter, namely Figure of Merit (FoM or FM), is defined to represent the helicopter efficiency. It is the ratio of ideal power required to the actual power in hover. C_{Pmeas} in here, includes both induced and non-ideal effects.

$$FM = \frac{P_{ideal}}{P_{meas}} = \frac{C_{Tmeas}^{3/2}/\sqrt{2}}{C_{Pmeas}} \tag{1.17}$$

It can be written by using the momentum theory as

$$FM = \frac{\textit{Ideal power}}{\textit{Induced power+Profile power}} = \frac{\frac{C_T^{3/2}}{\sqrt{2}}}{\frac{\kappa C_T^{3/2}}{\sqrt{2}} + \frac{\sigma C_{d_0}}{8}} \tag{1.18}$$

A typical efficiency graph is presented FM versus thrust coefficient. From a typical efficiency graph (Figure 1.2), it can be inferred that the FM value is increasing with the thrust coefficient and it starts to decrease due to increased profile drag after it reaches a maximum value which is approximately between 0.7 and 0.8 for high efficiency helicopter rotors.

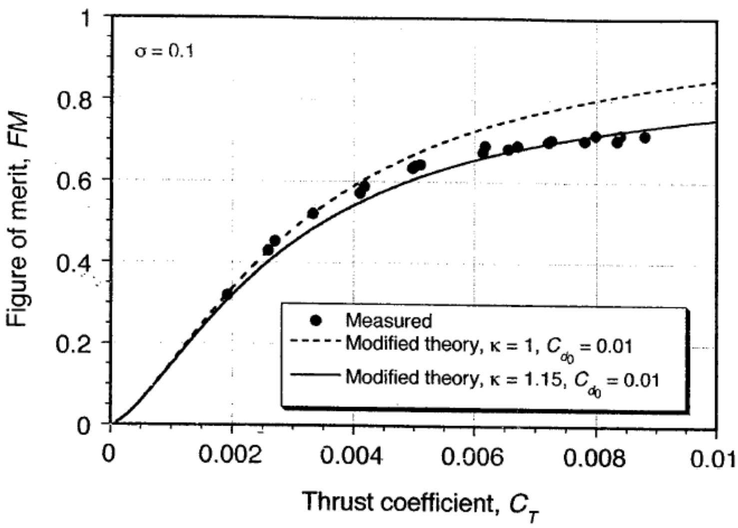

Figure 1.2: Typical FM graph with measured data and predictions [1]

1.1.2 Forward Flight

The rotor disc is tilted with an angle relative to the oncoming flow to produce both the thrust and a propulsive force to move the helicopter in forward direction. Rotor hub contains many complicated mechanisms such as swash-plate, pitch links and hinges to tilt the rotor and to control the aerodynamic forces. The amount of the thrust force is adjusted by changing collective pitch angle and the direction of thrust vector is adjusted by tilting the swash-plate which is named as cyclic pitch control. Besides mechanical complexity of the hub, there are aerodynamic issues during forward flight due to the asymmetric lift distribution on the rotor. As the helicopter begins to move in forward direction, some part of the rotor named as advancing side encounters the free-stream flow which is in the same direction as rotational velocity so that this side experiences relatively high flow velocity and thus higher aerodynamic loads; while the retreating side of the rotor is exposed to lower velocities and even reverse flow near the root. The differences between the flow fields on the rotor in hovering and forward flight configurations can be seen in Figure 1.3.

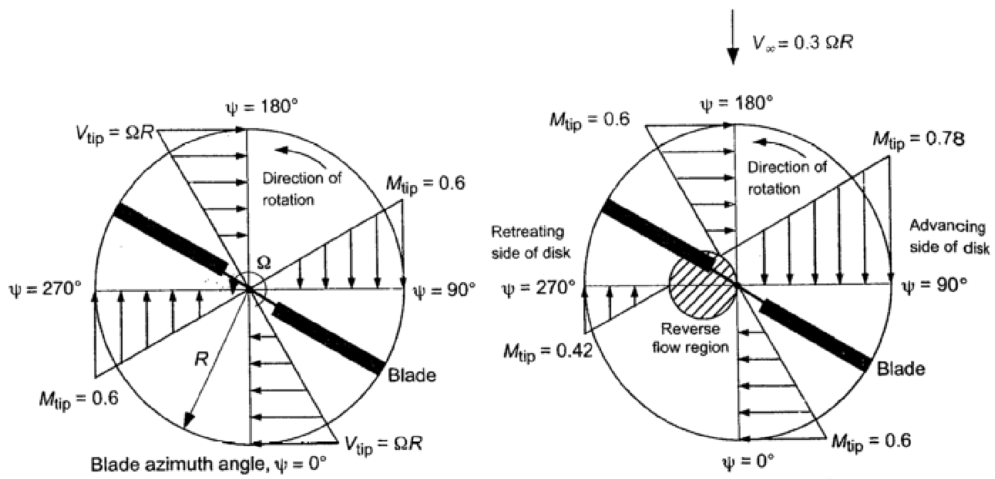

Figure 1.3: Flow field on rotor in hover (left) and forward flight (right) [1]

Higher velocities reached on the advancing side limits the tip speed of the helicopter in terms of compressibility effects. If the tip speed is high such that it exceeds the drag divergence Mach number, drag and thus the power requirement increases rapidly. The noise due to thickness of the blades, which is one of the types of the rotor noise, also increases proportionally with the increasing tip speed. In addition, some parts of the blades in advancing side may be subjected to transonic flow which results in wave drag, shock induced flow separation and high-speed impulsive noise.

On the retreating side of the blade, lower velocities are compensated with high angles of attacks which may result in dynamic stall of the retreating blade.

Because of different aerodynamic phenomena of hovering and forward flight, helicopters should be designed for an operational range rather than a specific design point like fixed-wing aircraft. That can be achieved mainly by a proper airfoil design. In addition to high lift to drag ratio, helicopter airfoil sections should have higher drag divergence Mach number for advancing side region, high maximum lift coefficients at low Mach numbers for retreating side region to maximise efficiency and they should have low pitching moment characteristics for easy control [1]. There is no optimum airfoil that ensures all of these requirements instead airfoil sections which satisfy these characteristics for a wide range of Mach numbers are preferred. To further increase the efficiency, special rotor blades having aerodynamic twist and modified tip shapes were developed. They will be explained in detail in the oncoming section.

Moreover, high speeds at the tip region of the blades form strong tip vortices. These tip vortices move in the downward direction in a helical shape due to rotation of the blades and create additional induced velocities in the wake of the rotor. On the contrary to the symmetrical wake and vortex trajectory in hover condition, vortices may interact with each other, blades or fuselage due to the combination of asymmetric wake and flow direction during forward flight. Aerodynamic issues about helicopters in forward flight can be summarized in Figure 1.4.

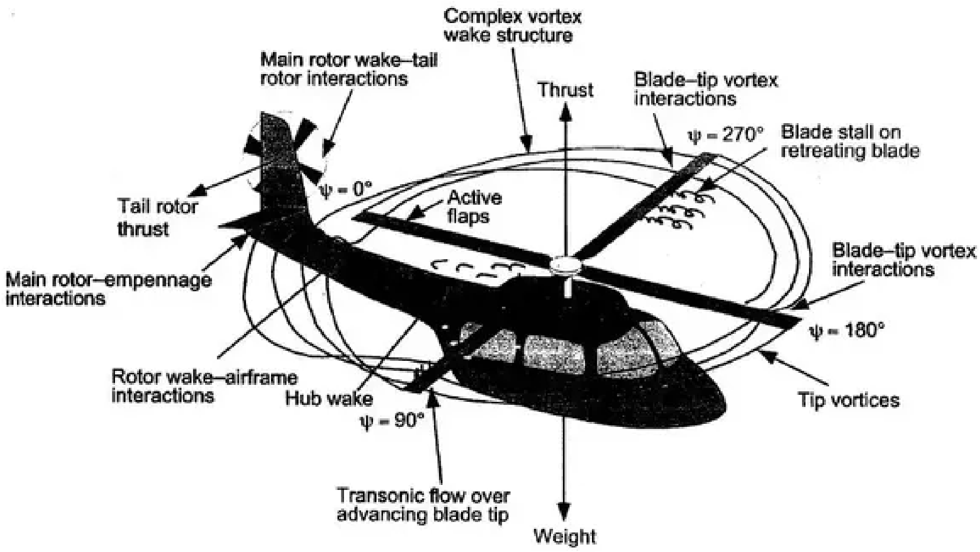

Figure 1.4: Complex aerodynamics of the forward flight [1]

1.2 Tip Vortex Phenomenon and Characteristics

Tip vortex is the rotary air flow structure at the tip region of the wing/blade due to the pressure difference between the lower and upper surfaces of the wing/blade.
For fixed wing aircrafts, tip vortices convect downstream in the wake of the wings, so that they have relatively minor influence on the free-stream flow. Moreover, the decrease of aerodynamic performance due to this three-dimensional flow structure around the wing tips is minimized to some extent by use of winglets. On the other hand, for rotary-wing aircrafts, such as helicopters, the tip vortices follow a rotary path and they produce a complex and unsteady flow field around the rotor. They also generate induced velocity which increases the power required in hovering flight. Especially in descending and forward flight, the tip vortices shed from rotor blades and they pass in close proximity to the same or different rotor blades at later times which results in Blade Vortex Interaction (BVI) noise besides the loss of aerodynamic performance. Therefore, the understanding of the tip vortex phenomenon becomes indispensable to predict rotor performance.

Tip vortex models are presented mainly by using 2-D velocity profiles since other velocity components are small to be neglected. The main parameters that regarding a vortex are its swirl (tangential) velocity, core radius, age and trajectory. Vortex core radius is defined as the distance between the peak tangential velocities (shown in Figure 1.5). The core is modelled as a solid body rotation, and the velocity which is outside of the core decreases hyperbolically as for a potential vortex. Vortex age or wake age corresponds to the azimuth angle of a vortex point relative to the blade from which it originates. Vortex trajectory is comprised of the radial and axial locations of the vortex center from the tip of the blade at different wake ages. Different parameters like circulation also can be calculated from that parameters and can be used to represent vortex strength.

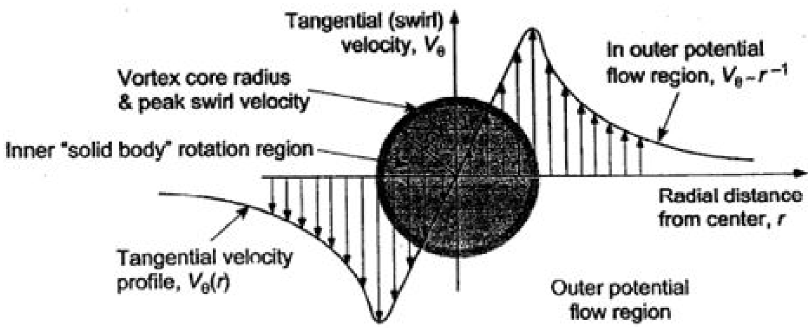

Figure 1.5: Demostration of the vortex core and tangential velocity profile [1]

Through the years, many experimental studies are performed to understand the tip vortex phenomenon, its effect on the rotor performance and to develop wake and vortex models for a more accurate prediction of the rotor aerodynamic performance. In the Table 1.1 experimental studies are given in a chronological order with their aim, method and flight conditions. By looking at the table, it can be said that starting from flow visualization, for many years, hot wire anemometry and laser Doppler velocimetry (LDV) techniques are used to measure flow velocities and obtain vortex dynamics. Use of the hot-wire anemometry technique decreased when the non-intrusive methods such as LDV came up. Even though LDV is a non-intrusive method and provides accurate measurement of velocity, it requires too much effort to acquire a complete velocity field since it is a point-wise measurement technique. After the development of image processing technology, PIV took the place of other techniques since complete velocity field can be observed easily and rapidly. It can be noticed that the number of studies performed in hovering flight is more than forward flight probably due to the simpler experimental setup and ease in observing a symmetrical flow field.

The below-listed experimental studies contributed to the fundamental understanding of the blade tip vortex characteristics. The earliest rotor performance prediction methods use uncontracted wake models which can not capture changes in the wake at different solidities, tip speed and thrust levels [7]. It has led to the need for an investigation of the wake geometry to accurately estimate wake models and performance. In one of these studies, Langrebe [7] performed flow visualization measurements for different blades and flight conditions, and formulated the wake axial and radial coordinates as a function of wake azimuth angle (wake age) and thrust coefficient. It was shown that the wake axial velocity and the wake contraction increases with increasing blade loading; however, the wake geometry is independent from the tip speed and aspect ratio. Moreover, it was observed that the wake becomes more unstable as it moves away from the rotor. Caradonna and Tung [10] carried out both blade pressure measurement and hot wire measurements to find vortex strength and trajectory, which are input for the prescribed wake lifting surface code. Vortex strength was defined as the ratio of vortex circulation to the maximum blade-bound circulation. Vortex parameters such as velocity, circulation and locations were found from hot wire measurements. The hot wire probe acquired many data along the estimated vortex trajectory with the help of a traverse system. The exact vortex location and the corresponding vortex velocity were found from the acceptable wake data where the probe hits the vortex core. They also found that the vortex trajectory and non-dimensional vortex strength are independent from tip speed. Tung and etc. [13] performed similar hot wire measurements together with the performance measurements which is done by the 6-strain balance mechanism to understand the effects of blade twist and aspect ratio on the vortex structure. They found no significant effect of blade twist and AR, however it was discovered that the vortex structure is similar to that found for fixed wing and it is comprised of four regions: a laminar inner region, a turbulent logarithmic region, a transition region, and an irrotational outer region. With the advance of non-intrusive methods like LDV, many studies focused on detailed vortex structure and changes in the vortex characteristics as it propages in the flow. Thompson and et al. [14] performed flow visualization and 3-component LDV measurements for a

Table 1.1: Experimental Studies about Tip Vortices

Year	Person	Aim	Method	Flight
1972	Landgrebe, A. J. [7]	Obtain wake geometry	Performance measurements on model rotor test rig& Flow visualization	Hover
1973	Tangler, J. L etc. [8]	Investigate vortex stability, tip shapes, compressibility and noise	Performance measurements on model rotor test rig by using strain gauges & Flow visualization & Hot wire	Hover
1978	Tangler, J. L [9]	Compare subwing's vortex structure with rectangular tip	Performance measurements on small-scale rotor test stand with strain gauges & Flow visualization & Hot wire	Hover
1980	Caradonna, F. X. & Tung, C. [10]	Predict blade loading by using vortex geometry and strength	Pressure measurements with test facility & Hot wire	Hover
1980	Rerry, U. & Raymond, E. [11]	Investigate the effects of several tip designs on the performance	Wind tunnel tests with articulated helicopter model rotor system & Performance measurements	Hover& Forward flight
1981	William H. W. [12]	Investigate the effects of blade tip geometry on loads and performance	Wind-tunnel tests of an aeroelastically designed rotor model with strain-gage balance	Hover& Forward Flight
1981	Tung, C. etc. [13]	Investigate the effects of blade geometry on vortex structure	Performance measurements in hover test chamber with 6-component balance& Hot wire & Hover performance codes	Hover
1988	Thompson, T. L. etc. [14]	Measure tip vortex core	Flow visualization & 3-C LDV with model rotor test facility	Hover
1995	Smith, D. etc. [15]	Identify specific tip shapes with high tip vortex diffusion capabilities	Wind tunnel measurements with 3-C Hot wire & Flow visualization	Fixed wing
1996	Leishman, J. G. etc. [16]	Investigate the vortex characteristics as it aged in flow	3-C LDV with model rotor test facility	Hover
1996	Mullins, B.R. etc. [17]	Examine the tip vortex strength of four tip shapes at high Mach and Re numbers	Pressure measurements in a transonic wind tunnel	fixed wing
1997	Iiurashige, A.& Tsuchihashi, A. [18]	Understand the PIV technique & tip vortex structure during BVI	Performance measurements on model test stand with strain gauges & 2-C PIV	Forward flight
1998	Leishman, J G. [19]	Measure aperiocity of vortex	3-C LDV	Hover
1998	Raffel, M. & Willert, C. [20]	Measure flow field of tip vortices & Comparison of LDV and PIV	3-C LDV and 2-C PIV with model rotor in a wind tunnel	Forward flight

Table 1.1 (continued)

Year	Person	Aim	Method	Flight
2000	Bhagwat, M.J.& Leishman, J. G. [21]	Investigate the structure of tip vortices for improved modeling	3-C LDV with model rotor	Hover
2000	Heineck, J.T etc. [22]	Gain experience in applying 3-C PIV & Obtain vortex core size and document the effects of vortex wander	3-C PIV with model rotor in a test chamber	Hover
2002	Burley, C. L. etc. [23]	Investigate vortex characteristics and find new methods for calculation of core size	3-C PIV with model rotor in wind tunnel	Forward flight
2002	Martin, P. B. etc. [24]	Document the essential physics of the trailing vortex as it aged in the flow	3-C LDV with model rotor test stand	Hover
2003	Kato, H. etc. [25]	Understanding of the tip vortex structure during the BVI	3-C PIV with rotor test rig in wind tunnel	Forward flight
2004	Han, Y. O.& Leishman J. G. [26]	Investigate the effects of slotted tip blade on vortex characteristics	3-C LDV and flow visualization with model rotor in a test cell	Hover
2006	Wall, B.G etc. [27]	Solve difficulties associated with the analysis of 3-C PIV measurements	3-C PIV	Forward flight
2006	Richard, H& Wall, B V. [28]	Investigate the development of tip vortices under different rotor conditions	2-C and 3-C PIV with model rotor in a test hall	Hover
2007	Ramasamy, M.& Leishman, J G. [29]	Identify the sources of uncertainty associated with the application of PIV	3-C PIV and LDV with model rotor	Hover
2009	Ramasamy, M. etc. [30]	Investigate the formation and evolutionary characteristics of the blade tip vortices	Dual-plane PIV (DPS-PIV) with model rotor	Hover
2011	Kindler, K. etc. [31]	Investigate vortex aperiodicity	3-C PIV with full scale rotor	Hover
2013	Mula, S. M. etc. [32]	Investigate dynamical characteristics of blade tip vortices over extended vortex ages	3-C PIV with model rotor test stand	Hover
2015	Nandeesh H. etc. [33]	Establish the nature of the Sharp-edge vortex	3-C PIV with model rotor in wind tunnel	Forward flight
2017	Bauknecht, A. etc. [34]	Observe the effects of actuation on tip vortices	3-C PIV with model rotor in a test chamber	Hover
2018	Shuilin, H. etc. [35]	Investigate the effect of anhedral blade on aerodynamic and aeroacoustic performance	Performance and sound pressure level (SPL) measurements on model rotor in an anechoic chamber	Hover

one-bladed rotor. From the flow visualization, they estimated the vortex trajectory and the vortex core size, which appears as a void region on the laser sheet, and they observed the unsteadiness of the vortex. They extracted the vortex axial and tangential velocity profiles as a function of radial coordinate along the vortex and compared with theoretical vortex models. In addition, it was reported that the void in the vortex core expands with increasing wake age and thrust coefficient, and the cycle-to-cycle fluctuation of the vortex location makes estimation of core size difficult. Leishman [19] also studied the aperiodicity of the vortex location in hover and it was found that the average aperiodicity is approximately 5% of the blade chord or about 50% of the core radius and increasing with wake age. Other 3-C LDV measurements which were performed for different wake ages [16], [21], [24] showed that vortices have a diffusive behavior. In other words, the vortex tangential velocity decreases logarithmically and the core size increases logarithmically with increasing vortex age [21]. In the detailed investigation of vortex formation and evaluation [24], it was observed that the vortex structure is neither fully laminar nor fully turbulent, it was composed of a region of relatively slow laminar diffusion and a region of accelerated turbulent diffusion. After the development of PIV technology, acquiring the whole velocity field became easier and faster, but still many studies [22], [23], [25], [27], [28], [29] were carried out to understand the application of the PIV and its uncertainties when observing vortex characteristics. Different averaging and vortex core detection methods were suggested in these studies to reduce the effect of meandering on the vortex characteristics. Since dynamic behaviour of the vortex is a key factor that determines the vortex center and its characteristics, recent studies focused on vortex meandering behaviour of full-scale and [31] model [32] rotors.

1.3 Literature Survey on Different Tip Shapes

For many years, the factors that enhance helicopter performance are investigated. The design parameters such as airfoil, number of blades, rotor radius, twist, pitch angle, advance ratio, etc. are optimized to reach maximum efficiency for a specific design range. Apart from these, there are always aerodynamic and acoustic performance losses due to the tip vortices (Section 1.2). Hence, to push the efficiency limits, some studies focused on that issue and tried to decrease the effect of tip vortex by modifying the blade tip geometries.

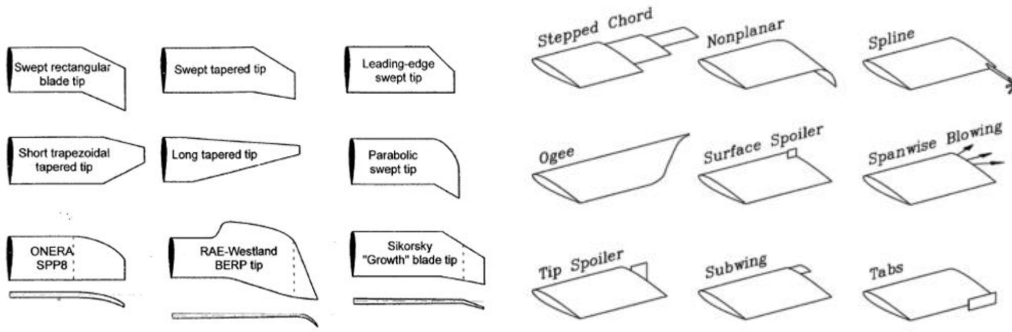

Figure 1.6: Different tip shapes [2]

The variety of the tip shapes (Figure 1.6) mostly comes from different flight conditions and design requirements. Broklehurst and Barakos [2] summarized helicopter rotor blade tip shapes together with their design purpose. From their paper, it can be interpreted that the tapered tip is used to improve the figure of merit in hovering flight since it has a lower profile drag for small tip Mach numbers. In addition, it helps to minimize the control loads and torsional deflections. However, as the tapered tip has a narrow tip chord, flow separation with higher profile drag may occur due to the lower chord Reynolds number. In forward flight and at high tip speeds, a swept tip is introduced in order to suppress the shock development on the advancing blade. One disadvantage of the sweep-back tip is that center of gravity (c.g.) is moved to the aft and it becomes distant from the aerodynamic center. In order to overcome that situation, a forward swept configuration is suggested. Anhedral tip changes the position of the tip vortex to more downwards in the wake and shows an increased aerodynamic performance.

Some advanced tip shapes which include combination of sweep, taper and anhedral were developed and produced within the long-term projects and collaborations. For example Blue-Edge^{TM} blade, which is designed for Eurocopter, uses a forward-backward sweep that reduces the BVI noise by 3-4 dB and it was validated with flight tests of EC155 [36]. The British Experimental Rotor Program (BERP) blade is designed especially to overcome the conflicting behaviour of advancing and retreat-

Figure 1.7: EC155 with the Eurocopter Blue-Edge^{TM} blade [3]

Figure 1.8: Westland Lynx with BERP blade [3]

ing side aerodynamics. It uses different and new airfoil sections through the blade. For example, thinner airfoil section having higher drag divergence Mach numbers is located at tip region. Large amount of sweep which relieves compressibility effects is balanced with forward notch offset that brings the c.g. forward. Moreover, its design intentionally forms stable vortex flows at high angles of attacks to delay the separation [1]. Later, anhedral angle is combined with BERP to balance the pitching moment variation caused by sweep and notch offset and and it is accepted that 20° anhedral increases the FOM by about 0.02 with no performance penalty in forward flight [2]. BERP blade was used in Westland Lynx, EH-101 and S-92 helicopters and it enabled the Lynx to gain the World Speed Record in 1986 with a speed of 400.87 km/h corresponds to a tip Mach number of 0.977 and with an advance ratio of 0.5 [2].

Some special passive and active tip shapes such as Ogee, sub-wing, split tip, vane tip, blowing tip, slotted tip, spline tip etc. (Figure 1.6) are designed specifically to reduce the vortex strength and the BVI noise by breaking up the vortex. However, it was found that their design causes an increased drag and power consumption; therefore, they are never used in full-scale helicopters.

As mentioned before in the Sections 1.1 and 1.2, tip vortices change induced velocity of the wake and affect the helicopter aerodynamic performance. So, the effects of different tip shapes on vortex characteristics is an important issue when the total performance is considered and maximum efficiency is desired. For this reason, many experimental studies focus on observing vortex characteristics for different tip geometries.

Tangler and etc. [8] conducted thrust/torque and hot wire measurements with a model rotor setup in hover and observed that the swept tip shows at least a 3% performance improvement over the square tip at medium thrust coefficients and they found that the double swept tip has the lowest vortex tangential velocity and the largest vortex core size. The Ogee tip was designed to decrease the effect of BVI and results showed a decreased vortex core intensity together with a reduced hover performance [37]. Weller [12] carried on performance tests with rectangular; swept; double swept with thickness taper; and swept with thickness taper, chordwise taper, and anhedral. It was reported that the configuration with anhedral gives the best aerodynamic performance in hover and at low advance ratios. For higher advance ratios, use of a sweep angle gives better results. Mullins and et al. [17] performed pressure measurements in a transonic wind tunnel with fixed mounted blades and order of performance from best to worst was presented as swept-tapered, swept, rectangular and tapered. They also observed that the swept and the swept-tapered planforms diffuse vortex more than the others. Smith and Sigl [15] tested 8 different passive and active rotor tip shapes in a wind tunnel to investigate their diffusion capabilities. It was found that active tip shapes such as NASA star and subwing result in vortex diffusion greater than 50% but they cause increased drag, therefore they should be retractable or variable geometry. Different tip shapes were tested with LDV by Martin and Leishman [38]. They observed that tip sweep dimishes both the radial and axial convection of the vortex, while taper increases the radial convection and decrease the axial convection. They also investigated the subwing and its vortex characterictics. Han and Leishman [26] designed and tested a new tip shape named as slotted blade which enables the air pass through the holes inside the blade and goes out at the tip region. Slotted blade reduced the peak value of the swirl velocity up to 60% relative to the baseline blade with a 3% increase in rotor power. Recently, the effect of anhedral angle ($20°$ and $45°$) on the figure of merit and aeroacoustic of a hovering model rotor was investigated [35]. The flow field was simulated by using a CFD code in order to explain the mechanism behind the improvement in the FOM and it was found that anhedral increased the distance between the vortex and rotor plane and reduced the vortex strength. Moreover, a drop in the rotor load noise was observed in the case of anhedral angle.

There are also computational studies which focus on the effects of different blades on aerodynamic performance and noise, and try to optimize the blade tip geometry. In their computational study, Yucekayali and et al. [39] tested swept, anhedral, taper blades and their combinations and found that double+swept+anhedral combination has the maximum BVI noise reduction besides relatively high aerodynamic performance but it has the highest peak-to-peak torsional moment variation. In the tip shape optimization study of Lee and et al. [40], although the double swept tip shows better noise results, the single swept tip is found to be more beneficial due to its lower dynamic load of pitch in hovering flight. Another study states that the 15° anhedral improves the figure of merit of the BERP blade (5.5%) more than a rectangular blade (4.4%) [41].

1.4 Objective and Scope of the Thesis

It is clearly seen from the previous studies that the optimum blade tip shape can vary for different rotor geometries and flight conditions. Moreover, it does not only affects the aerodynamic performance but also changes aeroacoustic and structural characteristics of the rotor. Therefore, the geometry of blade tip is still a goal of ongoing research to reach the fastest, the quietest and the most efficient helicopter. While experimental studies focus on measurements of rotor aerodynamics, aeroacoustic performance and investigation of the detailed vortex structure; computational studies concentrate on developing accurate aerodynamics and aeroacoustic performance prediction codes by using vortex models obtained from experimental studies and optimising the blade tip geometry via these codes. However, there are limited experimental studies on comparison of different tip geometries recently. The previous ones mostly were performed by using limited measurement techniques and compared the effects of tip geometries in terms of only performance or only vortex characteristics. Although there is a general idea about the effects of tip geometries on the aerodynamic performance, the underlying mechanism is still unknown.

The objective of this study is to investigate the effects of different blade tip shapes on the rotor aerodynamic performance and the tip vortex characteristics. In other words, it was aimed to understand the mechanism behind the changes in aerodynamic performance by observing vortex structure. Therefore, the study combines load (thrust and torque) and flow field measurements. In the first experimental campaign, a scaled 5-bladed rotor model was tested with different blade tip shapes by using thrust and torque sensors and aerodynamic load data were taken at different pitch angles and tip speeds. Secondly, phase-locked 2-component PIV measurements were performed between 0°-72° phase angles for the selected tip speed and pitch angle. PIV results were analysed with both phase averaging and conditional averaging methods. The effects of different rotor tip shapes on the vortex characteristics are also reported.

CHAPTER 2

EXPERIMENTAL SETUP AND METHODOLOGY

2.1 Background About Rotor Test Stands

Helicopter rotors are designed for specific ranges of Reynolds and Mach numbers. Although Mach number at the tip of the scaled rotor blade could be the same as the real helicopter by adjusting the rotational speed of the model, the chord-based Reynolds numbers of the full scale rotor and the model can not be equalized due to the geometric scale of the model rotors except for some special cases [12], [42]. Therefore, in many studies researchers perform experiments at the highest possible Reynolds numbers in laboratory conditions besides achieving full scale Mach number at the tip. Other than these aerodynamic concerns, complex hub design of a helicopter is another issue when designing a model rotor system. It is explained in Section 1.1 that helicopters adjust the amount of thrust force by changing collective pitch angle and adjust the direction of thrust vector for forward flight by tilting the swash-plate which is named as cyclic pitch. Model rotors are generally designed to operate at different collective pitch angles; therefore, their design should allow to change blade pitch angle manually or by using a collective pitch mechanism. When forward flight test is also desired, a swash-plate and hinge mechanisms (lead-lag, flap and feather hinges) are required in addition to the collective pitch mechanism. Another important issue is to measure aerodynamic forces created by the rotor and to transfer the data from a rotary system by using proper sensors and mechanisms. Since this study focuses on hovering flight, test setups which are designed especially for hover are investigated. Figure 2.1 shows some of the rotor setups which are capable of measuring aerodynamic forces in hover.

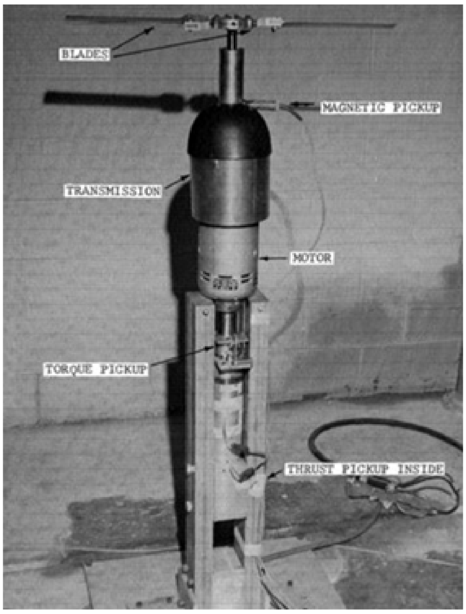

(a) Hover test rig [8]

(b) Rotary Wing Test Stand (RWTS) [22]

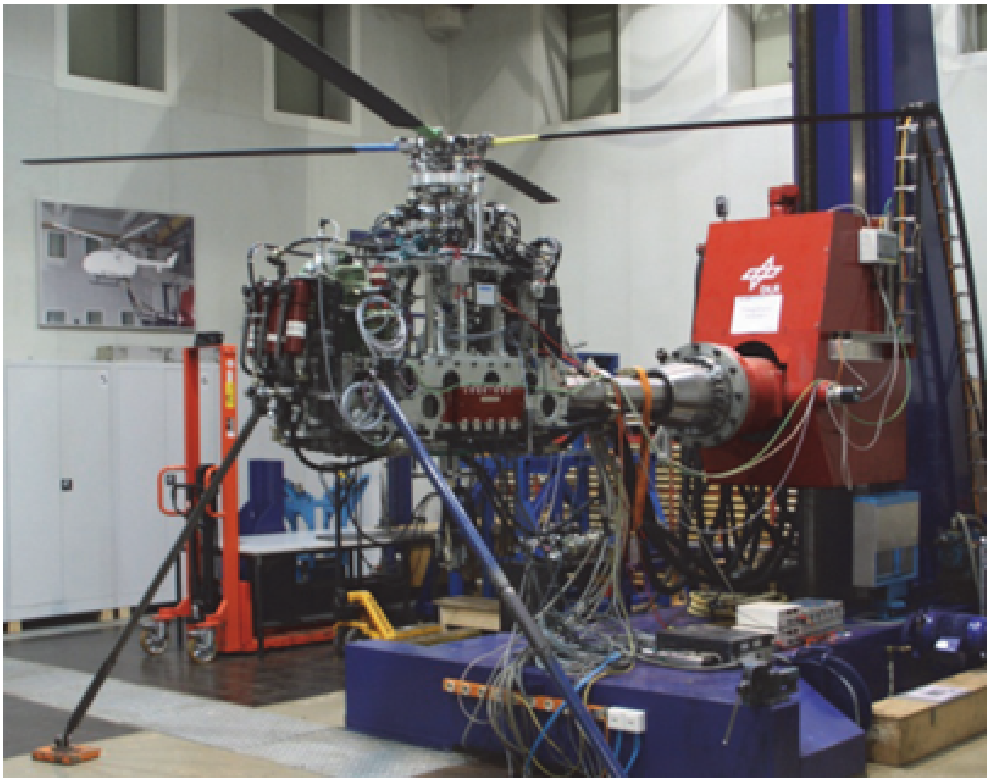

(c) The META test setup at the DLR's rotor test rig ROTEST II [43]

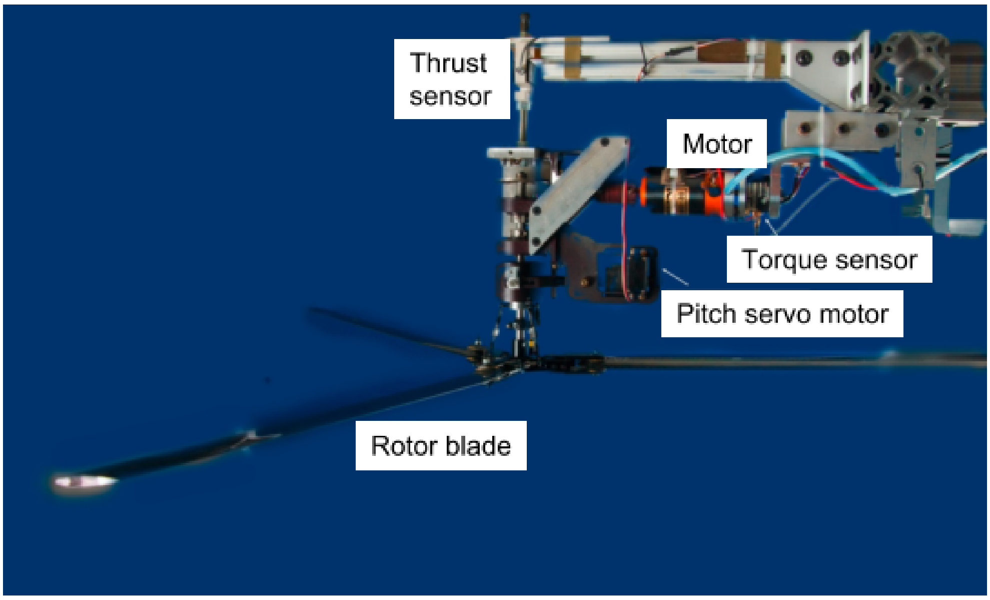

(d) Three-bladed rotor system [44]

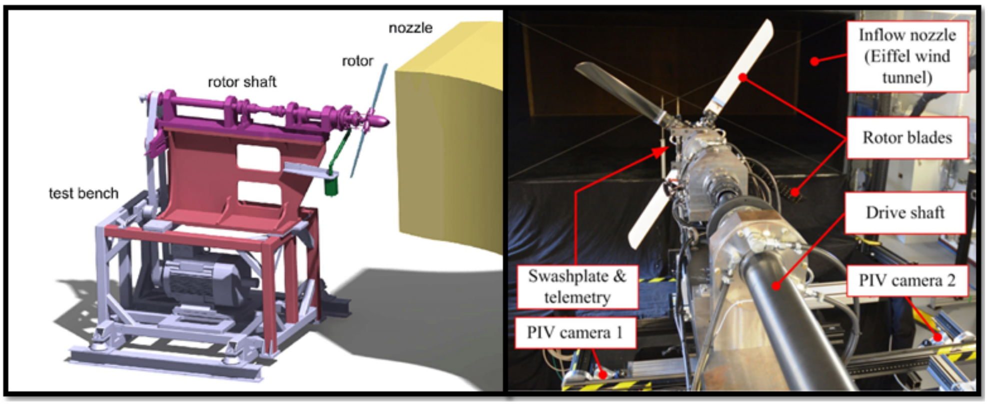

(e) The Rotor Test Facility Göttingen (RTG) [45]

Figure 2.1: Different rotor test setups from the literature

They have different designs and measurement mechanisms because of their individual design requirements. The test rig in (a) measures thrust by using a small strain-gaged cantilever beam placed at the base of the test rig. Thrust created by the rotor is transmitted to the strain-gage with the help of a sliding shaft. Torque measurements are performed by using strain-gage moment arm which can be seen in the figure. The rotor can reach tip Mach number of 0.6 which is similar to full scale case, by rotating the blades with a radius of 0.35 m with 6000 RPM. Test stand in (b) uses a flexible coupling between the shaft and the balancing system to measure torque.

Both the test stands in (a) and (b) adjust collective pitch angle manually. ROTEST II (c) measures all rotor loads by using a six component rotor balance and uses a slip ring system to transmit the loads. It has 4-bladed 40% Mach scaled hingeless Bo105 model rotor which can reach full scale rotor tip Mach numbers with its operation RPM of 1041. Cyclic and collective pitch angles are changed by using computer controlled actuators. A different measurement system is utilized in rotor system in (d). A thrust sensor which is placed along the axis of rotor shaft and a reaction torque sensor which is mounted behind the motor are used to measure total load and torque exerted by the system. The frictional losses created by transmission and bearings were estimated by applying a known torque with a dynamometer-based brake for each measurement matrix. Aerodynamic torque of the rotor is found by subtracting these values from the total torque. It uses a servo motor to adjust the pitch angle. In addition, Hall effect sensor and accelerometer are used to measure RPM and vibration. Rotor with a radius of 0.65 m operates at 800 RPM which is equal to a tip Mach number of 0.16. The test facility in (e) places the rotor vertically in order to prevent ground effect and to be integrated into an existing tunnel for dynamic stall research. The rotor head is composed of fully functional swash plate together with the mechanisms of flap and lead-lag motion for the simulation of axial flight besides hovering flight. It uses the 2 or 4 bladed rotor with a radius of 0.65 m which is planned to operate at 3000 RPM to reach realistic tip speeds ($M_{tip} = 0.6$). A Kistler Piezo-Dynamometer is mounted below the rotor head for unsteady six-component measurements of the overall rotor forces and moments, and a telemetry system is used in order to transmit the data from the rotating system.

2.2 The Design of the Experimental Setup

Similarly, for this study, it is considered to design a model rotor setup that works at the full scale tip Mach number. It has been determined to place the rotor vertically in order to provide easier access to the rotor and test equipment and to reduce ground effect. The hover test setup is placed in a room which is large enough to prevent recirculation effects.

2.2.1 Preliminary Design

The basic elements of the model rotor setup consisted of rotor, hub and motor. The rotor size was determined according to the scaled properties of T-625 rotor. Therefore, 10% geometric scaled 5-bladed model rotor with a radius of 0.65 m was chosen. One-half aspect ratio of the T-625 was selected to obtain higher chord-based Reynolds number, which results in a chord length of 0.08 m. Tip Mach number is directly related to the tip speed, which is rotational speed times rotor radius. It was calculated that motor rotational speed should be 3000 RPM in order to work at the full scale tip Mach numbers which is nearly 0.6. A 200 kW electric motor which can reach 3000 RPM rotational speed was used to drive the rotor.

For thrust measurements, a sliding table which carries the motor, the rotor and other components was designed. A load cell that connects the sliding table to the fixed part of the bench was used to measure the transmitted force created by the rotor. The direction of the flow that will be produced during operation was planned to be towards the area which is less disturbed by the components such as the motor and bearings for accurate flow field measurements. So that the direction of the thrust force is chosen towards the motor (Figure 2.2).

Torque and RPM measurements were performed using a non-contact torque meter mounted on the shaft close to the rotor. Radial and linear bearings were used for sliding and balance mechanisms. A schematic of the preliminary design is illustrated in Figure 2.2.

Radial bearings were chosen according to the maximum load which they can carry.

Maximum load occurs in the case of maximum unbalance when two of the blades are broken and it was calculated as 227.8kN. Due to the high load capacity and the ability to carry axial load in both direction, 32312-J2-QDF model double row tapered roller bearing was selected. For linear bearings, SCE-40-UU model was chosen.

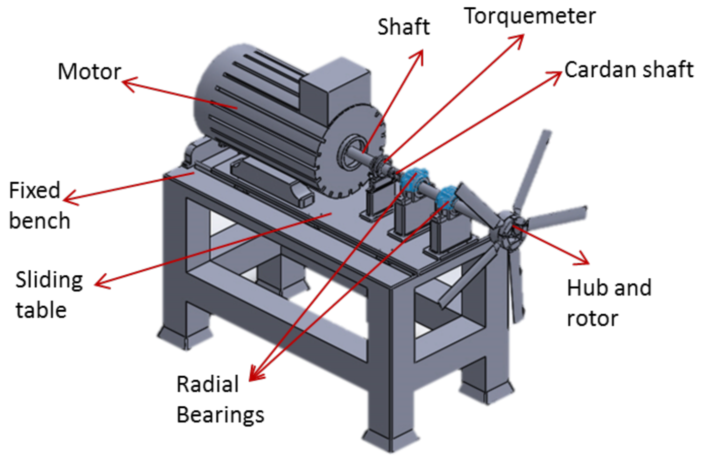

(a) Main components of the setup

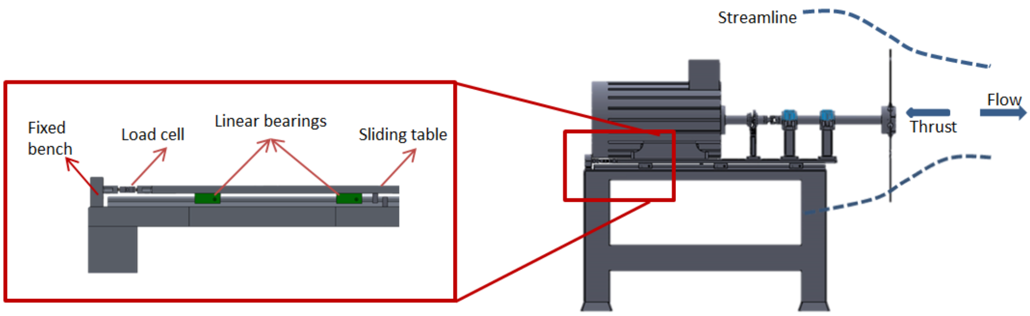

(b) The mechanism of thrust measurement

Figure 2.2: Preliminary design of the setup

2.2.2 Selection of the Sensors

In order to determine the range over which the load cell and the torque meter will operate, the maximum thrust and torque generated by the rotor at 3000 RPM was estimated up to 22 degree of pitch angle by means of numerical simulations [46]. Maximum thrust and torque values were found nearly 2500 N and 350 N.m (Figure 2.3). Therefore, HBM S9M (5 kN) load cell and K-T40B (500 N-m) torque meter were purchased. In addition, Kyowa AS-10HB (±10g), 1-axis accelerometer was obtained to monitor vibration levels of the system. Sensors can be seen in Figure 2.4.

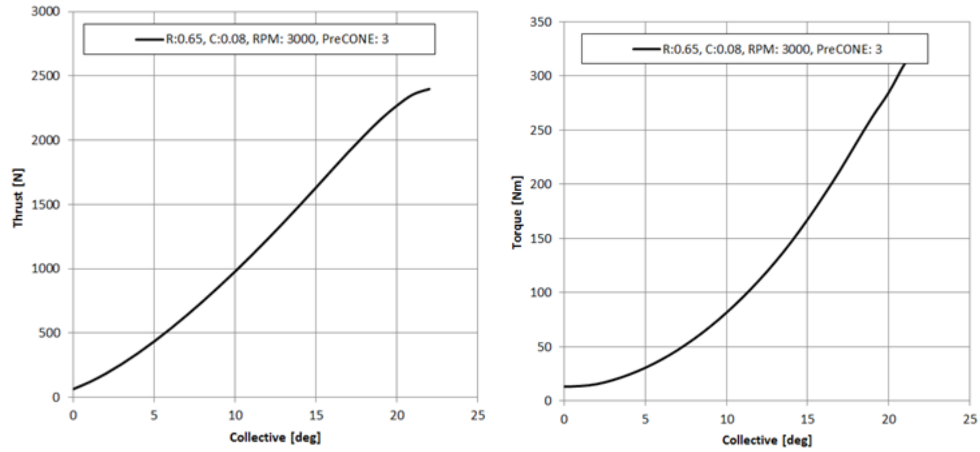

(a) Pitch vs. Thrust (b) Pitch vs. Torque

Figure 2.3: Performance analyses

(a) HBM K-T40B torque meter (b) HBM S-type S9M load cell (c) Kyowa AS-10HB accelerometer

Figure 2.4: Instrumentation

2.2.3 CFD Analysis of the Setup

Turkish Aerospace helicopter group [47] performed CFD simulations by using CFD++ in order to see the effect of bench including motor and bearings on the rotor performance and the flow field. The rotor is modelled as a disc. The surface grid of the bench, grid of rotor disk and volume meshes are generated with the software Pointwise with triangular unstructured elements. Results show that the bench does not affect the performance levels significantly (Figure 2.5) but front legs and bearings distort the flow field and the symmetry of inflow velocity distribution (Figure2.6). These negative effects were minimized in the final version of the setup by increasing the distance between the bench and the rotor in addition to modifying the front legs.

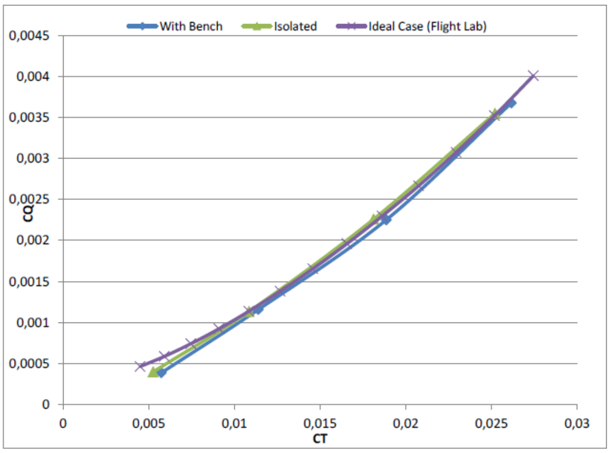

Figure 2.5: Thrust coefficient (C_T) vs. Torque coefficient (C_Q)

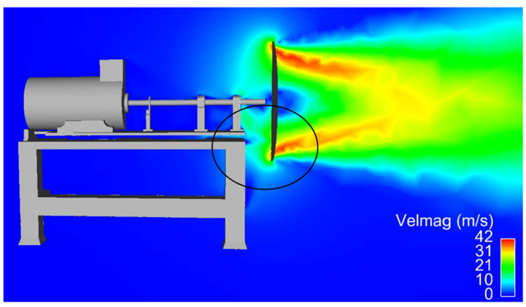

(a) Distortion of the symmetry of inflow velocity distribution

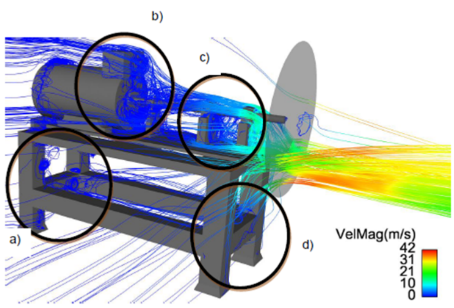

(b) Flow Distortion zones a) Back Legs , b) Motor , c) Shaft Connections , d) Front Legs

Figure 2.6: CFD simulations of the rotor test setup

2.3 Design of the Rotor

Since it is a hover test stand, there is no need for dynamic swash plate to allow cyclic pitch but the collective pitch of the blades should be still variable. The rotor design was need to be as simple and compact as possible since the rotor works at high RPM levels. Therefore, it was preferred to adjust the pitch angles manually rather than use of a pitch control mechanism. The hub is composed of three parts: hub base, blade holders and cap. 2 degree of precone angle in the direction of thrust was added into the hub base and the holder design in order to increase aerodynamic efficiency and decrease fatigue. TKK B 60x90 model locking bush, which can both shrink and expand when the screws on it were tightened, was used for the connection of the hub to the shaft. Five blades were mounted into the hub through their roots. The blade root was designed as concentric cylinders which have different diameters for strong connection, and placed between the hub base and the blade holder by using four screws of 8mm diameter. Blades were designed without twist distribution for easy manufacturing. The 3D drawing of the rotor and its parts are shown in Figure 2.7. The rotor properties are given in Table 2.1).

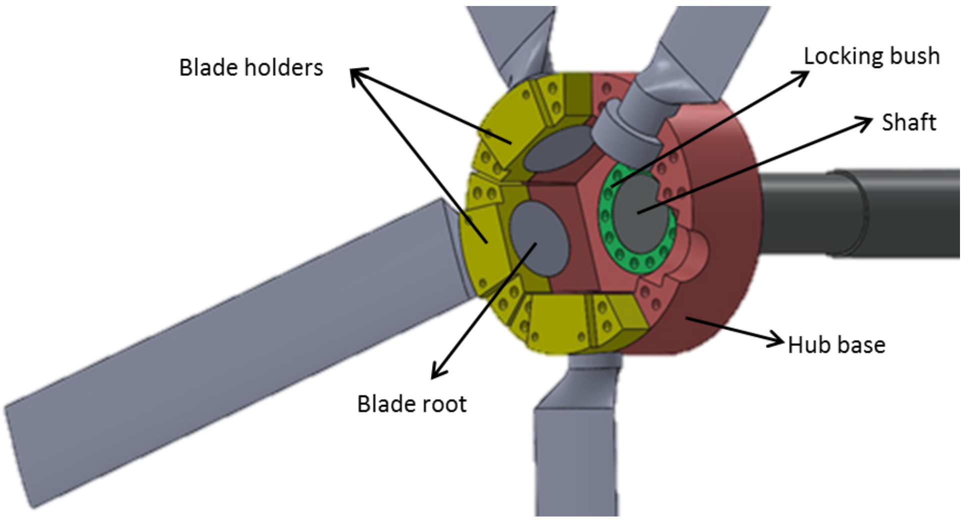

Figure 2.7: Rotor design and its parts: Blades, shaft, hub base, blade holders and locked bush. The cap is not seen in this figure.

Table 2.1: Rotor properties

Number of blades	5
Airfoil profile	VR7
Rotor radius	0.65 m
Blade length	0.535 m
Blade root cut out	0.115 m
Chord length	0.08 m
Aspect ratio	8.125
Solidity	0.16
Precone angle	2 °

2.3.1 Structural Analysis of the Rotor

After the design of the hub and blades, stress analysis of the rotor was done with the assigned material in order to check whether that rotor design can handle at high RPM (3000 RPM) levels with the chosen materials. The stress analysis was carried out at RUZGEM by using Abaqus [48]. The material of the hub base was assigned as steel and others was assigned as Al 7075. The interaction of steel and aluminium was simulated by using 'surface-to-surface' option. Moreover, 'tie' option was used between the parts and screw holes to connect the parts. Then appropriate boundary conditions and rotational body force were applied on the blade. It was found that the maximum stress of 146 MPa occurred at the inner corner of the hub base and screw connections and the maximum stress of 92 MPa occured at the blade region where closer to the blade root (Figure 2.8). When the yield and tensile strength of the material (505 and 570 MPa) were divided into these maximum stress values, factor of safety was found between 3-5. Since the safety factor is high, the material of the hub base also was chosen as Al 7075 T6 as it is lighter than steel.

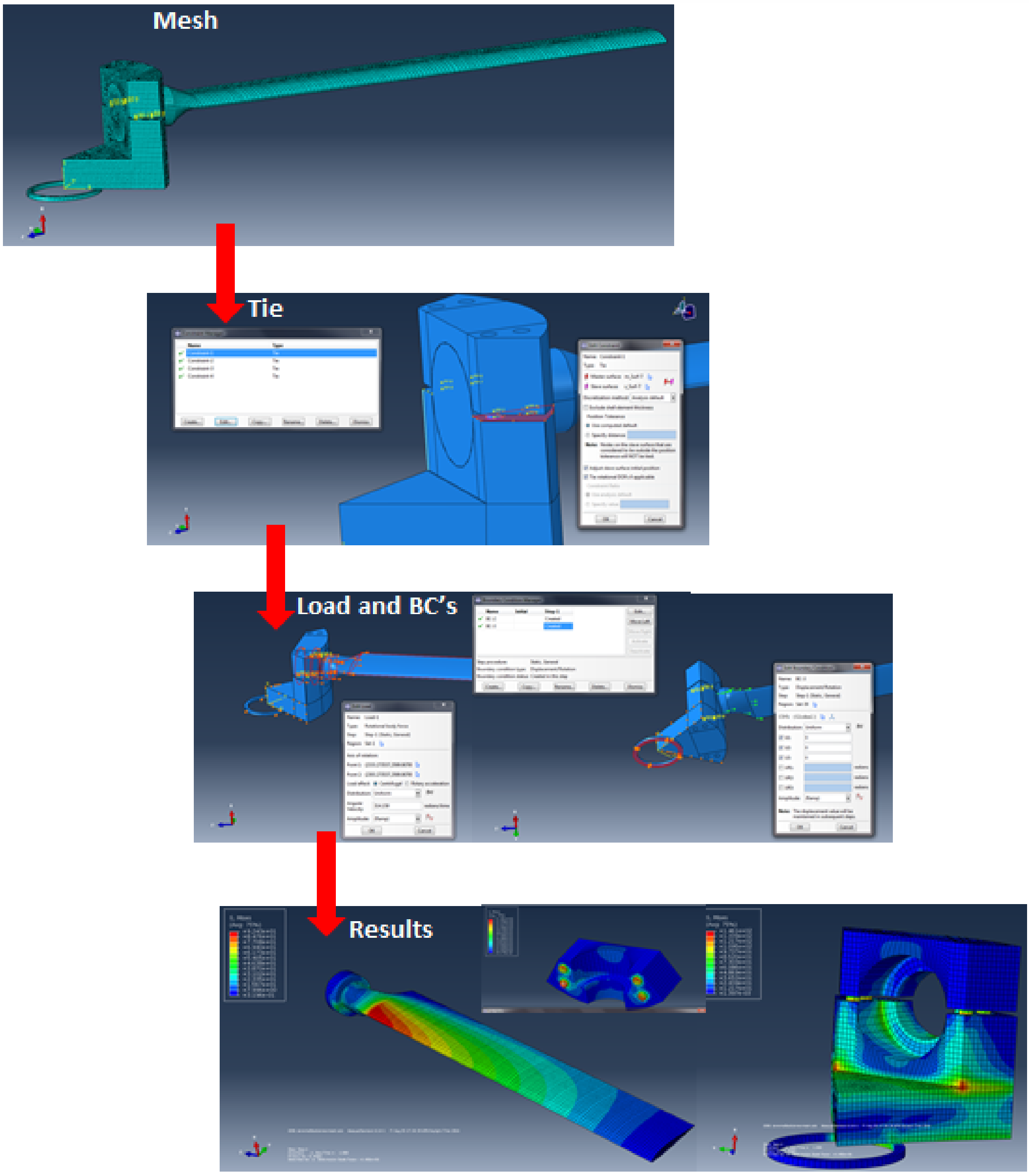

Figure 2.8: Stress analysis of the rotor [48]

2.3.2 Tip Modifications

Three different blade geometries were chosen in collaboration with Turkish Aerospace helicopter group considering previous tip shapes which are studied in the literature (Section 1.3). Tip design modifications were made in the area 0.1 R away from the tip of the blade. Anhedral angle was selected as 15°, sweepback angle was applied as 20° and taper ratio was chosen as 0.6 (Figure 2.9). Modified blade names are abbreviated as shown in the Table 2.2 and will be presented in this way in the results section.

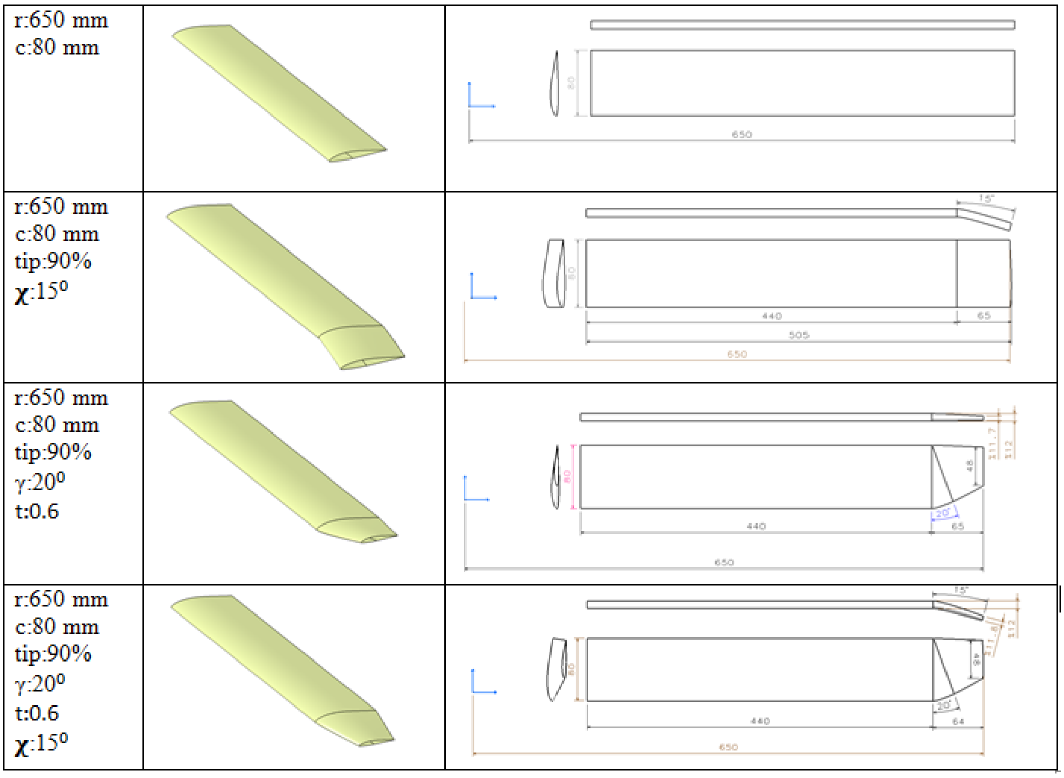

Figure 2.9: Drawings of the blades a) rectangular (baseline), b) anhedral, c) swept-tapered, d) swept-tapered-anhedral

Table 2.2: Definitions of different blades

Rectangular	RECT
Anhedral	ANHD
Tapered + Swept	TAPER
Tapered + Swept + Anhedral	TSA

2.4 Final design of the Setup

The hub and blades were manufactured (Figure 2.10) with selected materials. The manufacturing tolerance is ± 0.04 mm. As mentioned in the Section 2.2.3, several changes were made according to the CFD results. Cardan shaft was replaced with coupling mounted between the shaft and the torque meter. Bearings were covered and front legs were modified in order to reduce the interactions with the flow. The distance between the rotor and the bench was increased. Moreover, a protection wall having the size of 2×2.4 m and 58 mm thickness filled with 50 mm rock wool between the steel plates of 4 mm, was constructed around the rotor as a precaution against the risk of failure (Figure 2.12). The setup can be seen in Figure 2.13.

Figure 2.10: Fabricated hub and blades a) swept-tapered-anhedral, b) swept-tapered c) anhedral, d) rectangular (baseline)

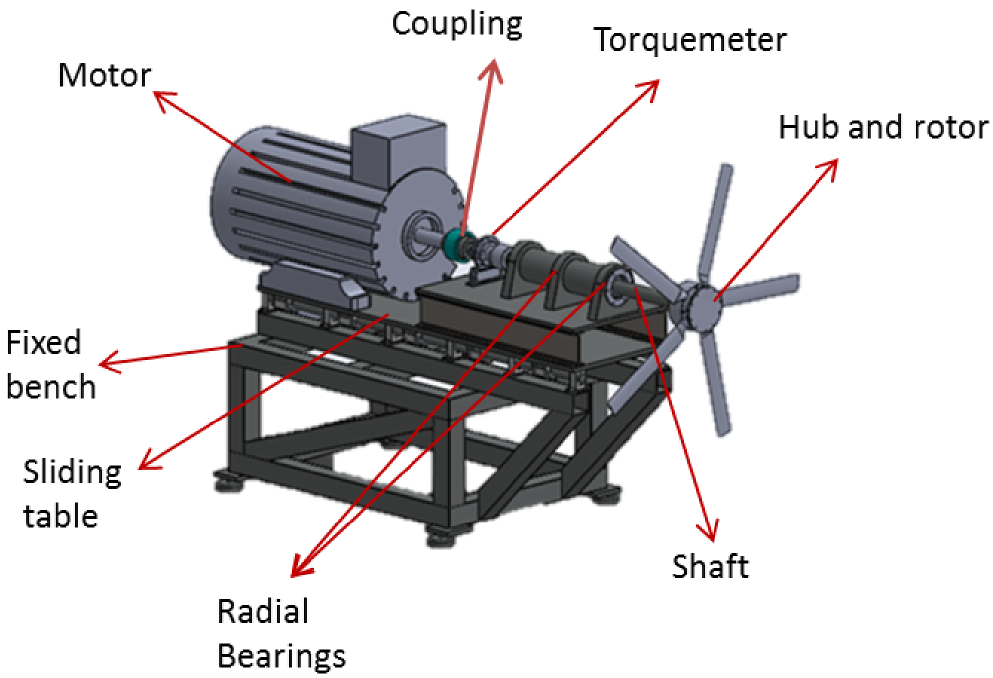

Figure 2.11: Final design of the setup

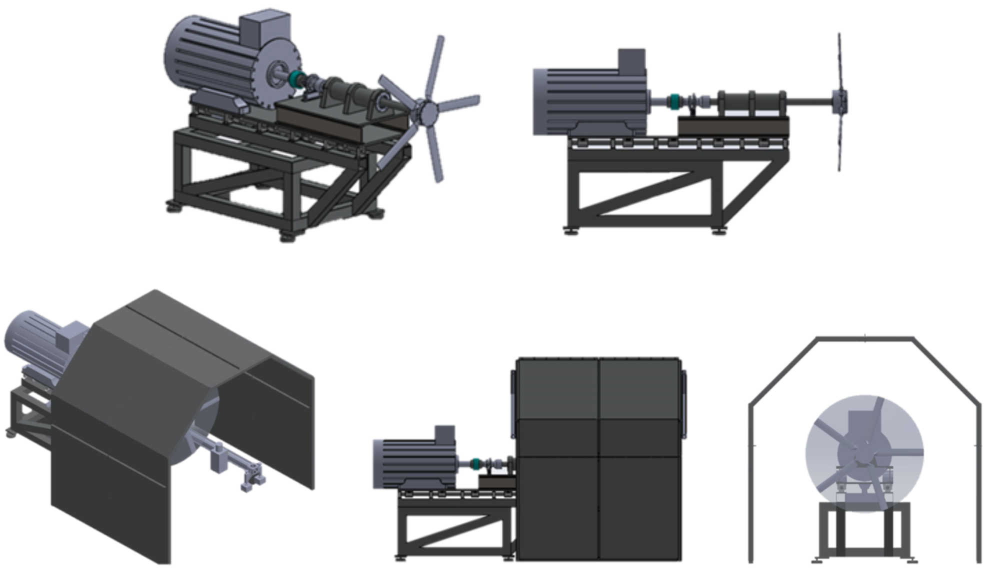

Figure 2.12: Different views of the final sketch of the setup

Figure 2.13: The setup

2.5 Characterization of the System

Since this rotor setup is a new design, number of measurements and analyses were done to reveal and understand its characteristics. These measurements were performed with rectangular blades at 5.8° pitch angle. It is necessary to balance the rotor before operation against the risk of different blade weights which may create asymmetry in centrifugal force distribution. Therefore, rotor balancing was done by a balance company (MBS) after every blade configuration was mounted, 4 times in total.

2.5.1 Alignment and Vibration Analyses

Even 1 mm misalignment in rotary systems can lead to increased deformation and eventually failure at high RPM levels. Therefore, some analyses and experiments were performed without operating the motor in order to check whether manufacturing tolerances, alignment of the system and vibration levels are within limits. First of all, Turkish Aerospace rotor group modelled the shaft by using Dymore and made analysis in whirl mode [49]. The whirling is defined as a circular motion of the deflected shaft center line about its undeflected position with a small amplitude. An unbalance mass of 125 grams was connected to the rotor to create asymmetry during the analyses and the maximum shear force which corresponds to critical shaft speed was calculated with increasing RPM. Shaft critical speed was found as 3600 RPM which is below the maximum allowable motor speed. Then, impact tests for modal analysis were carried out on the manufactured shaft in two symmetrical directions. It was observed that 3 peaks of natural frequencies occur at 27 Hz, 35.5 Hz and 58 Hz which correspond to 1620, 2100 and 3500 RPM. The peak at 3500 RPM matches with the shaft critical speed. Although the shaft is symmetrical, one peak at 12 Hz (720 RPM) occurred in the y direction which is an indicator of a misalignment in that direction. After that, the exact location and exact value of misalignments were measured by using a laser shaft alignment system (ROTALIGN touch) and positions of the motor, shaft and bearings were rearranged according to the allowable alignment tolerances.

Critical acceleration value of the system was determined according to the table taken from ISO 10816 mechanical vibration standard for rotary machines (Figure 2.14). The test setup can be accepted as category 3 or 4. The critical vibration velocities correspond to these categories are 11 mm/s and 18 mm/s respectively. Vibration velocity was converted into acceleration by using the maximum frequency (1000 Hz) given in the ISO 10816. After conversion, critical acceleration range were found as 7.04 g-11.54 g.

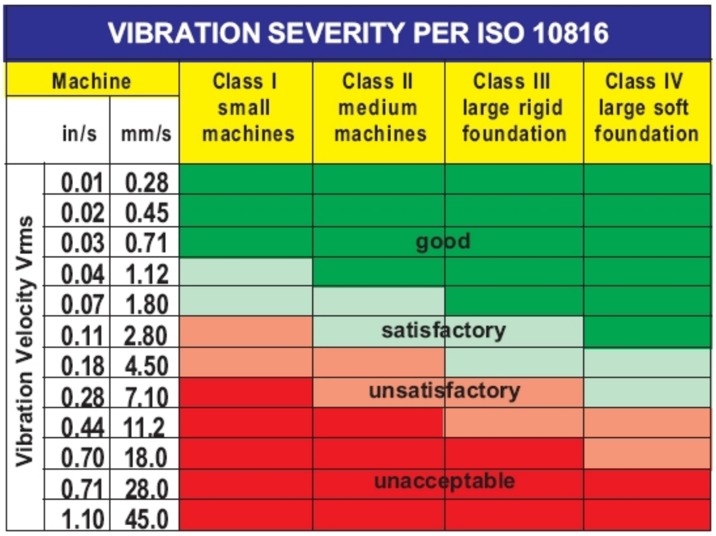

Figure 2.14: Vibration limits for rotary machines

Then, a single axis accelerometer was placed at different axes on the bench near the motor and vibration data was captured instantaneously with increasing RPM. Results showed that the vibration level increases substantially with increasing RPM and the dominant vibrations occur in y and z axes (Figure 2.15). It can be seen from the figure that the maximum vibration level is approximately 5 g at 2000 RPM with the blades having 5.8° pitch angle. Moreover, it was noticed that higher pitch angles that generate higher aerodynamic forces have an increasing effect on the vibration levels. The vibration levels reach to approximately 7 g ,which is very close to the limit, at 2000 RPM at the pitch angle of 20°. Therefore, the maximum allowable RPM was chosen as 2000 RPM for this study which corresponds to $M_{tip} = 0.4$. Furthermore, it was observed that when the blades are adjusted to zero pitch angle, mechanical vibration and noise levels increased significantly. It may be due to the gaps created by excess tolerated parts when combined with the lack of aerodynamic force. So that, zero pitch angle eliminated from the test matrix.

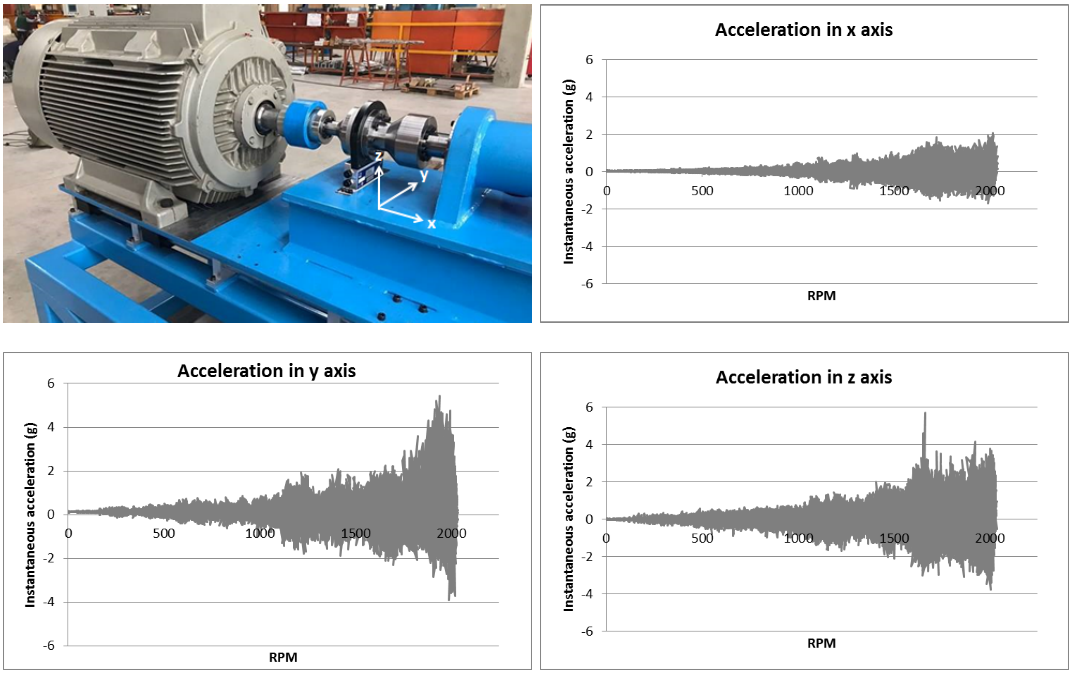

Figure 2.15: Instantaneous acceleration data during the operation of 0-2000 RPM

After these analyses and alignments, it was observed that Fast Fourier Transform (FFT) analysis of the accelerometer data at 2000 RPM, create peaks at every 33 Hz (2000 RPM) and there is no other peak which indicates misalignment. (Figure 2.16).

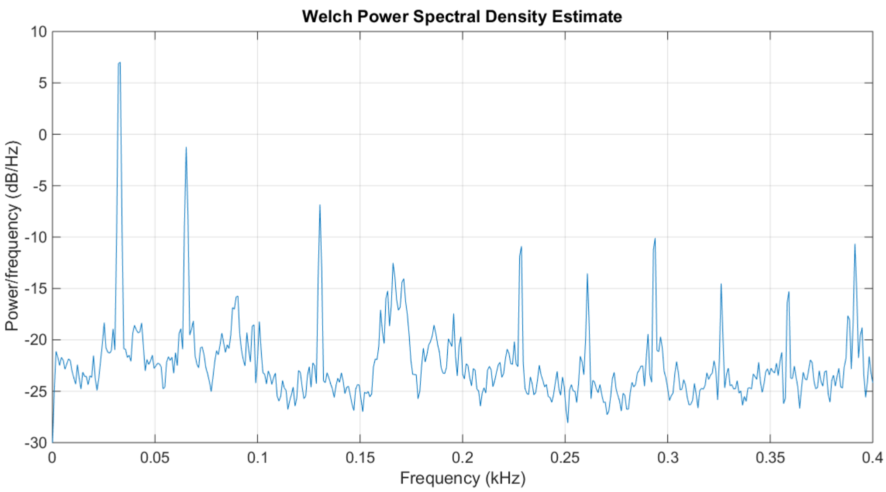

Figure 2.16: FFT analysis of accelerometer data at 2000 RPM

2.5.2 Calibration of Thrust Measurements

As explained in Section 2.2.1, the thrust generated by the rotor is transmitted to the load cell via a sliding table. It was found that the load cell reads lower load values than the applied firce on the rotor due to extra resistance of the bearings on the sliding table mechanism. Therefore, a thrust calibration was performed. Objects having different weights were hanged to the center of the rotor with the help of a pulley system and corresponding forces were measured and recorded by the load cell. It was found that there is 25% loss on the system (Figure 2.17). That loss was added to the load measurements after the experiments to estimate the rotor thrust.

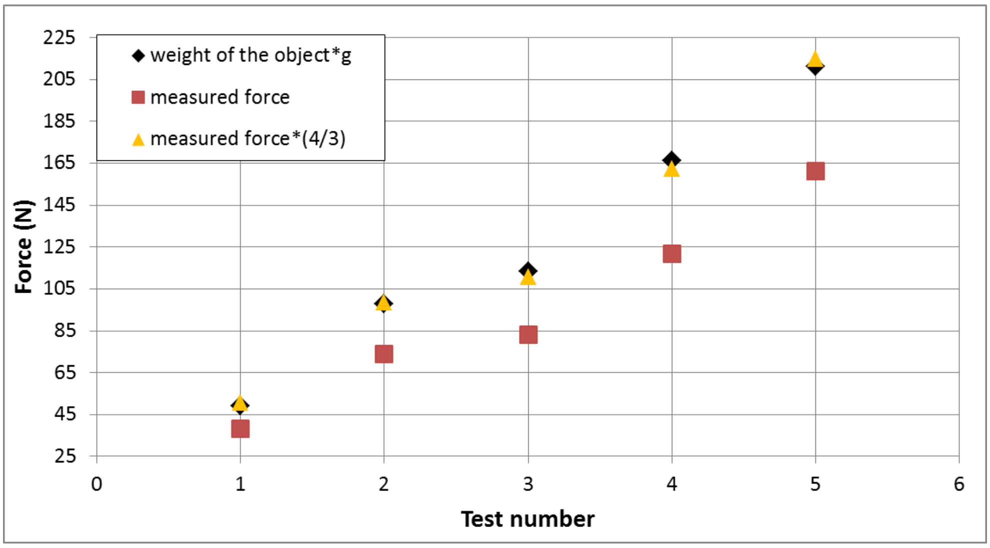

Figure 2.17: Calibration of the force measurement system

2.6 Measurement Details

In this section, measurement details and measurement matrix of the thrust/torque and PIV measurements are presented. Number of samples and sampling frequency are optimized to get precise and time saving performance measurements. The properties of the PIV measurements such as number of images, time interval between two laser pulses, laser power etc. are determined by checking the quality of images and vectors.

2.6.1 Thrust and Torque Measurements

Thrust and torque measurements were performed at two different tip Mach numbers (0.3 and 0.4), at five different pitch angles (5.8°, 12°, 16° 18°, and 20°) and for rectangular, anhedral, swept-tapered and swept-tapered-anhedral blade geometries. Measurement matrix can be seen in Table 2.3. Humidity, pressure and dew point values were recorded for each measurement and used to calculate air density. RPM was adjusted based on the changing temperature in order to keep the tip Mach number at the desired value. Sensors were set to zero before every measurement. Thrust and torque data were taken during 1 min at 2400 Hz sampling rate after waiting for a minute at the required RPM value. It was determined to take five measurements in order to check repeatability and to perform averaging to decrease the level of random error. Finally, thrust and torque coefficients were calculated by using thrust, torque, air density and RPM for each measurement.

Table 2.3: Test matrix of thrust and torque measurements

Blades	M_{tip}	Re_{tip}	$Re_{tip,taper}$	Pitch Angle
RECT	0.3	470000	282000	5.8°
ANHD	0.4	630000	378000	12°
TAPER				16°
TSA				18°
				20°

2.6.2 Flow Field Measurements via PIV

Two dimensional - two component (2D2C) PIV system consists of a New Wave Research Solo 120-XT Nd:YAG laser with a wavelength of 532 nm, a maximum repetition rate of 15 kHz, and a pulse energy of 120 mJ/pulse in addition to a Phantom v640 camera with a maximum resolution of 2560×1600 pixels at a frequency of 1.5 kHz (4 megapixels at full resolution). Laser beam direction was changed by using mirrors and it was converted to a laser sheet at the quarter chord of the blade tip by using spherical lenses. The time interval between two laser pulses was selected as 15 μs. Camera was placed perpendicular to the laser sheet. 3-D traverse system which carries the camera and laser, was used to adjust the field of view at the tip region. The field of view has a size of 294 mm×184 mm, which corresponds to a scale factor of 10.75 pix/mm. A fog generator was used to fill the room where the rotor setup is located. The PIV recording parameters are summarized in Table 2.4.

Table 2.4: PIV recording parameters

Field of view	294×184 mm
Interrogation area	64×64 pixel
Dynamic spatial range	DSR≈ 40:1
Dynamic velocity range	DVR≈ 320:1 with two iterative multigrid
Object distance	690 mm
Recording Medium	Phantom v640 high speed camera, 2560×1600 pixel
Recording Method	Double frame- Single exposure
Recording Lens	$f = 60$ mm, $f_{\#} = 2.8$
Magnification factor	0.095
Illumination	Nd:YAG laser, 120 mJ/pulse
Pulse delay	15 μs
Seeding material	Glycol-water solution, $d_p \approx 1\ \mu m$

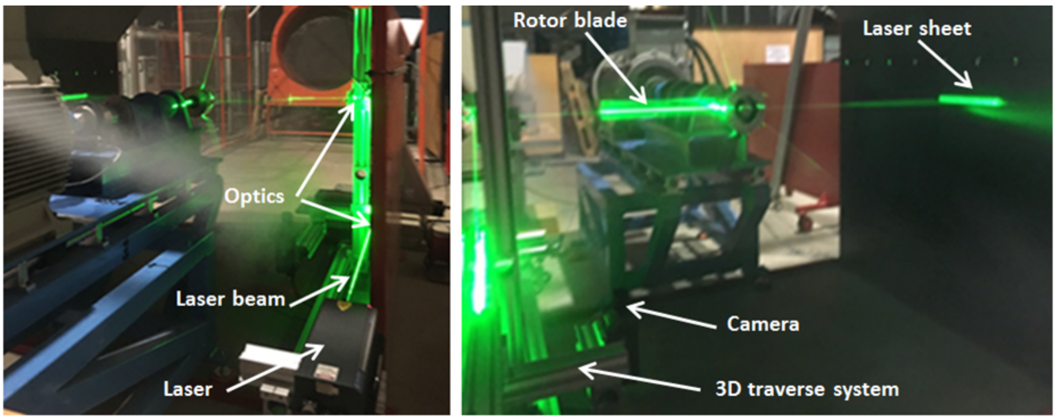

Figure 2.18: PIV system in two different views

Phase-locked measurements were performed in order to observe vortex trajectory and characteristics. Figure 2.18 shows a picture of the test facility while performing the PIV measurements at the rotor phase 0°. In this method, the PIV system and the rotor azimuth angle were synchronized by using a Hall effect sensor attached to the rotor shaft. This sensor sends one-per-rev signal to the synchronizer box. Then, the laser and the camera can be triggered at the predetermined azimuthal positions of the rotor by selecting a proper trigger time delay from DANTEC Dynamic Studio software. The experiments were conducted at 6° intervals between 0° -72° phase/wake ages. Phase 0° is defined as the azimuthal position of the rotor in which the laser cuts the quarter-chord of a pre-specified blade at the tip and it is accepted as the location of the vortex formation. Therefore, the position of the following blade corresponds to the 72° wake age of the vortex created from the first blade. The definition of the phase/wake age can be seen in Figure 2.19. The PIV measurements were conducted at the tip Mach number of 0.4 and 16 degrees of pitch angle for the baseline and three different blade geometries. For each measurement/phase, 1000 image pairs were recorded. It can be seen from the one of the recorded images that measurement window can capture three vortices which have 72° phase differences between them (Figure 2.20), i.e. a new tip vortex forming at the tip of the blade and two other vortices that are shed during the last two blade passages.

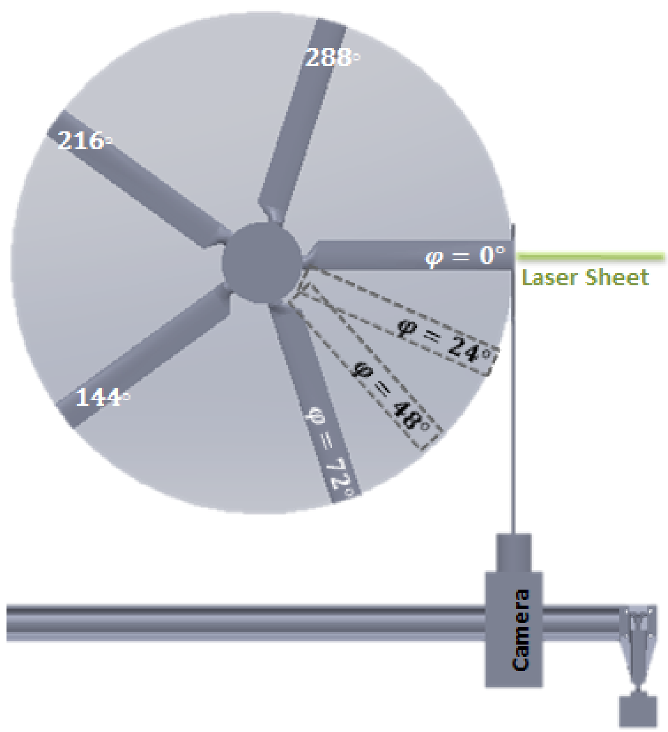

Figure 2.19: Phase angle definition

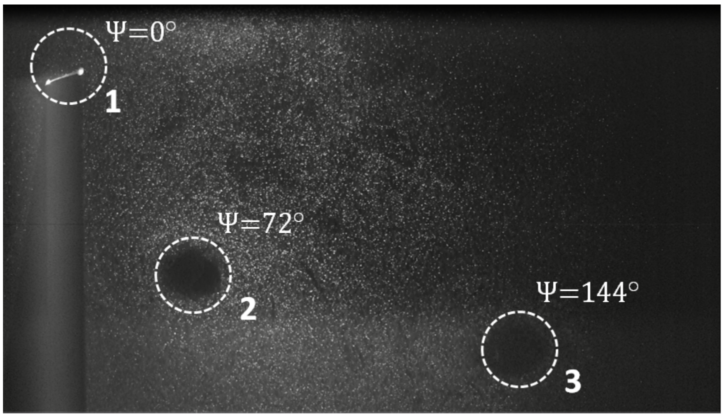

Figure 2.20: PIV raw image at $\phi = 0°$

2.6.3 Post-Processing Methods

Blade was masked and background subtraction was applied to the raw images in order to enhance the image quality. There are a few particles in the center of vortices due to the centrifugal force and it can be seen as a void in the Figure 2.20. It becomes difficult to find accurate vortex center and velocities. Therefore, although smaller interrogation window size is suggested for higher resolution, for this case larger interrogation window size, which is 64×64 was used in the cross-correlation process in order to increase particle numbers and vector quality in the calculation area. Cross-correlation method with interrogation area size of 64×64 pixel with 50% overlap resulted in a 3.44 mm vector spacing in both directions forming a dataset of 79×49 velocity vectors in the measurement plane. Moving average validation in a 3×3 neighbourhood was conducted on the vector maps before calculating the vector statistics. Finally, ensemble and conditional averaging were applied to the vector fields. Post processing steps can be seen in Figure 2.21. Vorticity calculation from the velocity vectors was performed by using Tecplot and presented as vorticity contours in the result section.

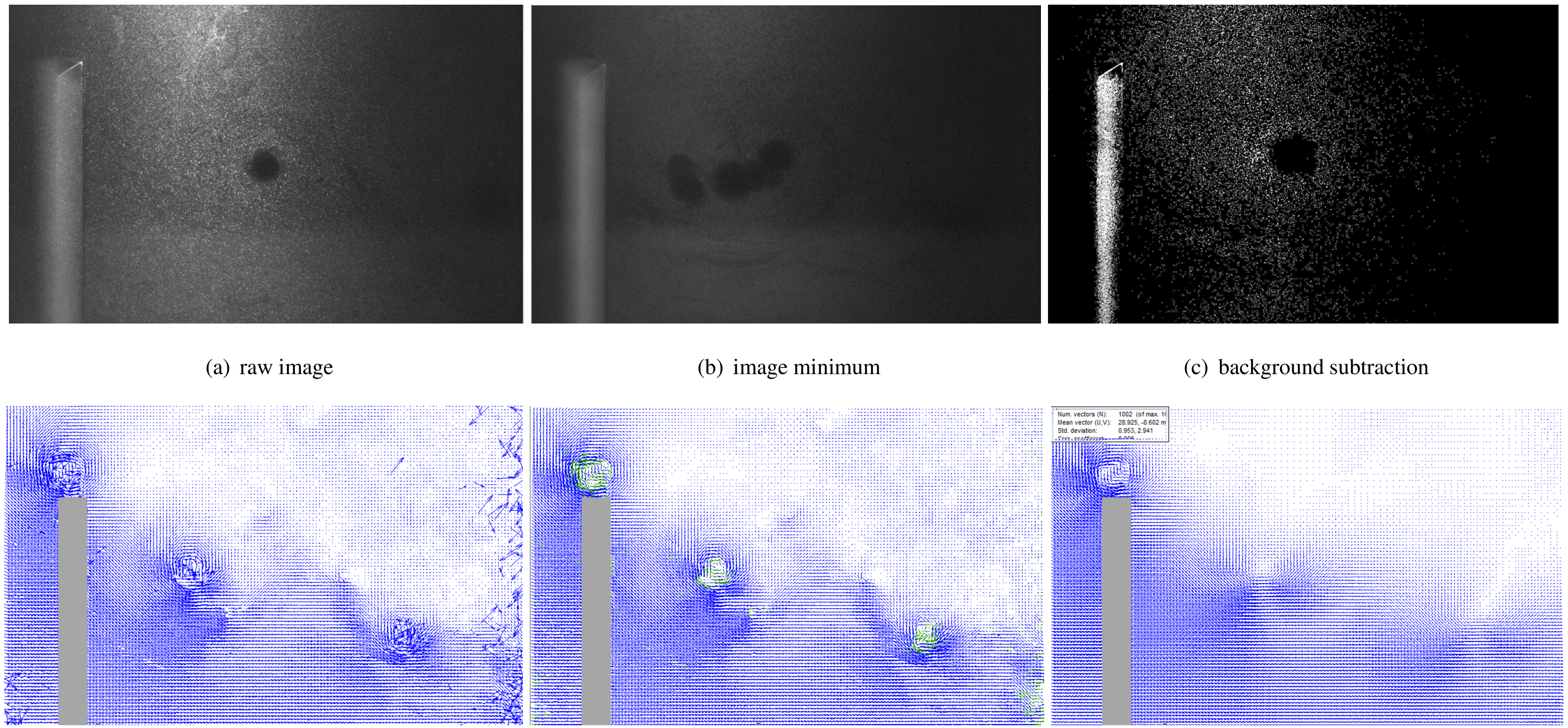

(a) raw image (b) image minimum (c) background subtraction

(d) cross-correlation (e) moving average validation (f) ensemble averaging

Figure 2.21: Post-Processing steps

2.7 Analysis of Measurement Errors

2.7.1 Accuracy of the Thrust and Torque Measurements

Random error levels for the thrust and the torque measurements are estimated by use of a statistical approach, in which cycle averaged thrust and torque values are used to calculate the uncertainty level in the presented mean values. The uncertainty of the RPM data is too low, therefore it is neglected. The uncertainties of thrust and torque data were calculated for different measurements and blades. The presented mean thrust and torque values have an uncertainty of approximately 0.1$\%$ and 0.5$\%$, respectively, with $\%95$ confidence level. A decrease in the uncertainty level of torque measurements was observed with increasing C_T and Mach number.

Since figure of merit calculation contains C_T and C_Q, its uncertainty level was calculated by using propagation of error formula (Equation 2.1). FOM values have an uncertainty level of less than 0.5$\%$.

$$\sigma_{FOM}^2 = \sigma_{C_T}^2 \left(\frac{\partial FOM}{\partial C_T} \right)^2 + \sigma_{C_Q}^2 \left(\frac{\partial FOM}{\partial C_Q} \right)^2 \tag{2.1}$$

2.7.2 Accuracy of the PIV Measurements

2.7.2.1 PIV measurement accuracy

There are some design rules regarding PIV measurement accuracy. For example, it is suggested that there should be at least 10-15 particles in an interrogation area for a higher vector detection probability and at least 1 pixel particle image diameter is recommended in order to prevent peak-locking phenomenon. Moreover, the maximum dynamic velocity range and peak-to-peak ratio is desired for accurate results [50]. Peak to peak ratio is the ratio of first peak height to the second peak height in the correlation map, which is obtained as a result of the cross-correlation of the interrogation areas at two consecutive time steps. It can be seen from Figure 2.22 that there are nearly 60 particles in an interrogation area except the vortex core region which suffers from poor seeding and particle size is almost 1.3 pixel which is above the risk of peak locking. Dynamic velocity range is found as 320 with multi-grid iteration. Peak height ratios are calculated by using the built-in function in the commercial PIV software Dynamic Studio from Dantec Dynamics. Figure 2.23 shows a selected raw image, its vector field after cross-correlation and the contours of peak to peak ratio values. Peak ratios near the vortex core is lower due to the void there. The rest of the velocity field have peak ratios between 3-6 which is enough for a high accuracy.

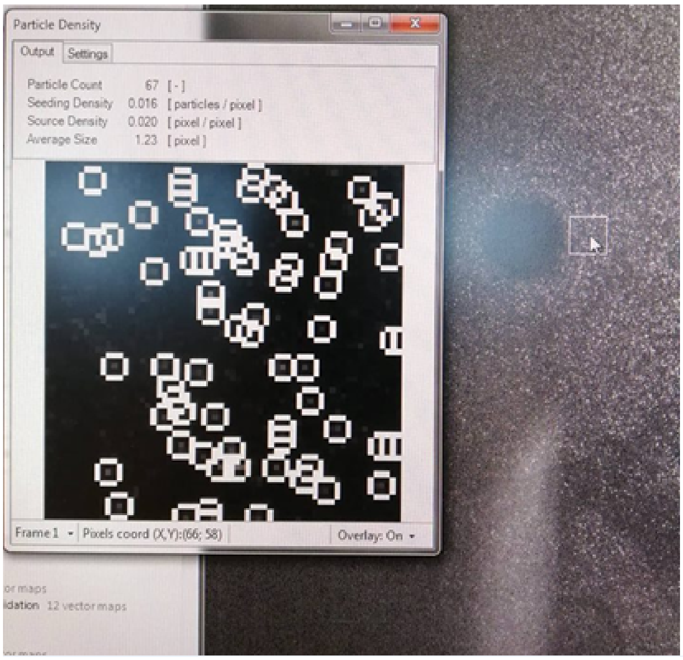

Figure 2.22: Particle properties

2.7.2.2 Uncertainty in velocity vectors

The working principle of the PIV technique is to find velocity vector by dividing particle displacement to time interval. Thus, random uncertainties mostly occur during the determination of the displacement in pixels from raw images. Many parameters, including particle image size, intensity-density, turbulent fluctuations, velocity gradients, noise level and interrogation window size, affect the determination of particle image displacement and their total uncertainity is reported between 0.05-0.1 pixel for many experimental configurations [51]. By selecting 0.1 pixel uncertainty with 15 μs pulse time, the uncertainty of velocity vectors is found as 6.6 pix/s (0.6 m/s) and the uncertainty of the induced velocity (25 m/s) is calculated as 2.4% for this study.

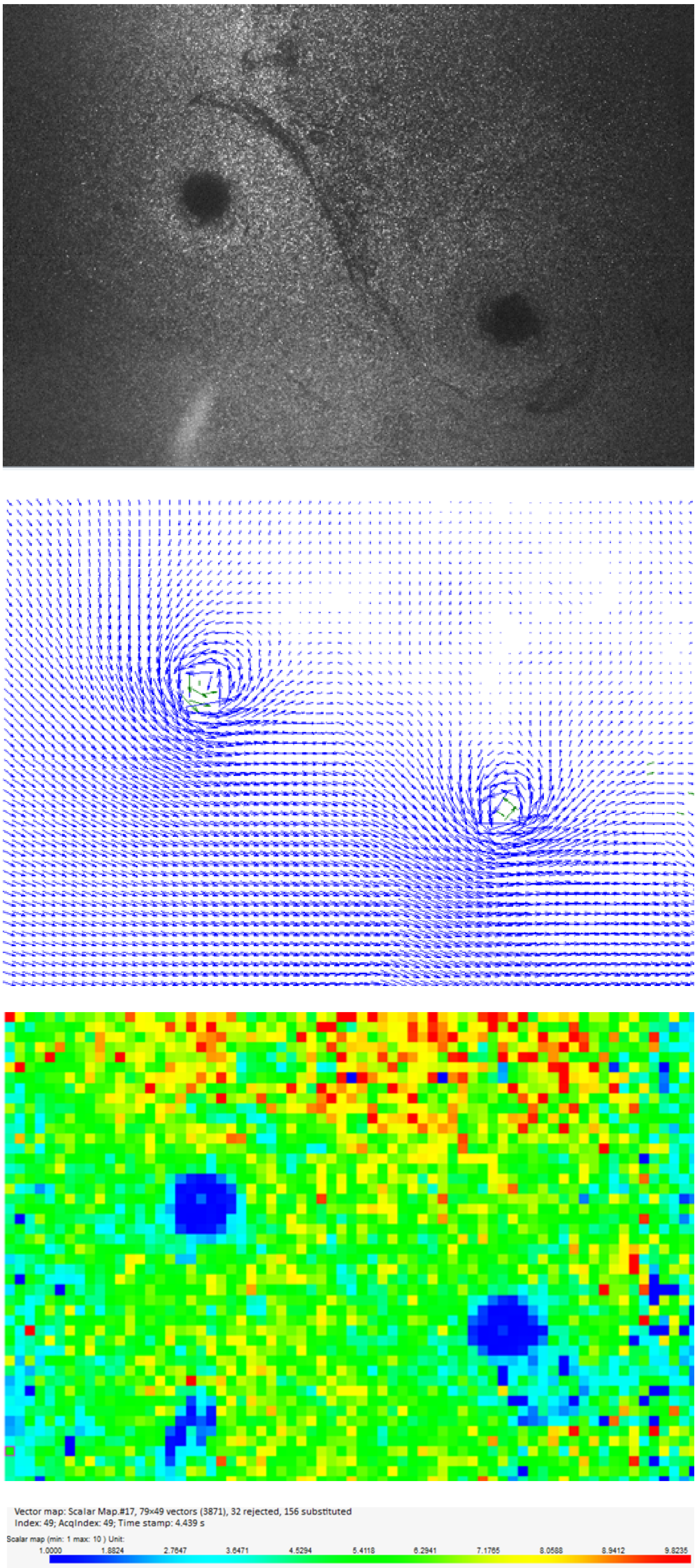

Figure 2.23: First peak to second peak height

2.7.2.3 Other sources of error for presented values

In 2-D PIV, laser sheet and flow component to be measured should be parallel to each other. In other words, for an accurate detection of vortex tangential velocities, the laser sheet should cut the helical vortex tube without inclination. One should calculate or estimate vortex trajectory for each wake age in order to correct the sheet orientation or velocity vectors. In this study, the camera was placed perpendicular to the laser sheet passing through the quarter chord of the each blade. In that position laser sheet has an angle of 16° with the blade due to the pitch angle but the tip vortex forms according to the effective angle of attack, which is less than 16°. Moreover, it is expected that the tilt angle changes as the tip vortex moves downstream in the wake in hover condition. Since the exact inclination between the laser sheet and the vortex through the helical trajectory can not be known for this study, it is assumed to be negligible similar to the previous studies performed in hover condition [32] and all the experiments were performed at the same described location.

CHAPTER 3

RESULTS AND DISCUSSION

In this chapter, results of the load (thrust and torque) and the PIV measurements are presented and discussed. First of all, load measurements will be compared to theory in order to examine the aerodynamic consistency of the rotor. Then, the load data will be plotted as dimensionless aerodynamic coefficients to interpret the aerodynamic performance at different tip Mach numbers and pitch angles for four blade configurations. In the second section, post-processing and vortex detection methods applied on PIV images will be described and vortex characteristics (vortex trajectory, vortex velocity profiles, vorticity and circulation) will be given at different vortex ages for all blade configurations.

3.1 Load Measurement Results

3.1.1 Comparison with BEMT

Blade element momentum theory (BEMT) is highly used to predict aerodynamic performance of many model or full-scale rotors. For this study, a BEMT code for 5-bladed rotor in hover condition written in Matlab. After the blade was divided into 40 sections, airfoil characteristics were extracted from XFoil for each section by using corresponding local Reynolds number, Mach number and airfoil profile. The formulas of local lift and drag coefficients are given by [1],

$$c_l = a(\alpha - \alpha_0) = a\Big(\theta - \frac{\lambda}{r} - \alpha_0\Big) \tag{3.1}$$

$$c_d = c_{d_0} + d_1\alpha + d_2\alpha^2 + ... \tag{3.2}$$

Where a is the 2-D lift curve slope of the airfoil, α is the angle of attack and is defined for helicopters as collective pitch angle (θ) minus inflow angle (λ/r). α_0 is the angle when lift is zero in the c_l-α graph. r is the radial station and d's are the constant coefficients of drag equation. They were found from XFoil except the inflow velocity (λ). The non-linear inflow velocity which includes Prandtl tip loss factor (F) was chosen for the calculations (Equation 3.3).

$$\lambda(r) = \frac{\sigma a}{16F}\left[\sqrt{1 + \frac{32F}{\sigma a}\theta r} - 1\right] \tag{3.3}$$

where σ is solidity and defined as, $\sigma = Nc/\pi R$
N: Number of blades
c: Chord length
R: Blade radius
F is the Prandtl tip loss factor which is also depends on inflow velocity so that it was calculated iteratively.

$$F = \frac{2}{\pi}\cos^{-1}(\exp(-f)) \tag{3.4}$$

$$f = \frac{N_b}{2}\left(\frac{1-r}{\lambda}\right) \tag{3.5}$$

The sectional thrust and torque coefficients for untwisted, constant chord blades in hover condition are given by,

$$C_T = \int_0^1 \frac{\sigma}{2} r^2 c_l dr \tag{3.6}$$

$$C_Q = C_P = \int \lambda dC_T + \int_0^1 \frac{\sigma}{2} r^3 c_d dr \tag{3.7}$$

Thrust and torque can be calculated by inserting Equation 3.6 and 3.7 into the below relations.

$$T = C_T \rho A (\Omega R)^2 \tag{3.8}$$

$$Q = C_Q \rho A (\Omega R)^2 R \tag{3.9}$$

where ρ is air density, A is rotor disc area and (ΩR) is the tip speed.

The theoretical thrust and torque values were calculated according to these formulations and compared with the measured values at $M_{tip} = 0.3$ for different pitch angles in Figure 3.1. It was found that the torque values of BEMT are slightly below the measured torque values which is expected since 3-D flow effect can not be included in theory. The theoretical thrust values are close to the experimental load data. Small differences can be due to again the 3-D flow effect. The comparison shows that the test setup is working properly and provides reasonable rotor performance results.

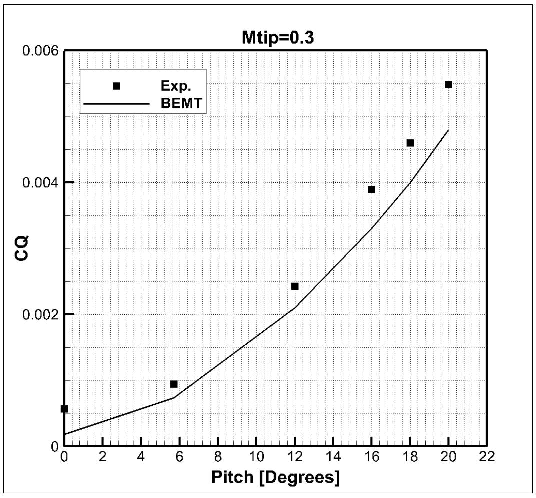

(a) Pitch vs. Torque

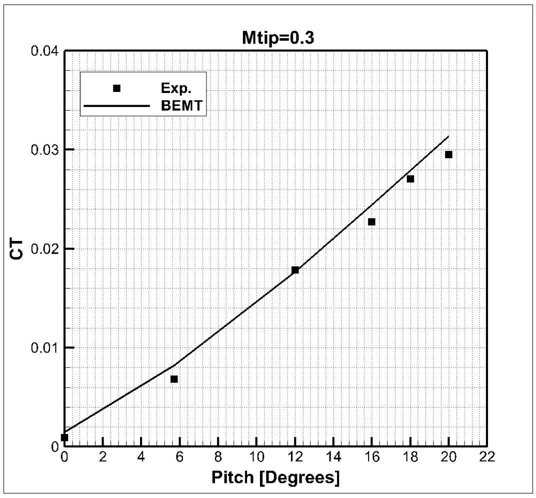

(b) Pitch vs. Thrust

Figure 3.1: Comparison between the measurements and BEMT

3.1.2 Aerodynamic Performance Graphs

Thrust and torque data were taken for four tip shapes and transformed into dimensionless coefficients by using the equations 3.8 and 3.9. C_T and C_Q were divided into solidity factor since blades have different tip chord lengths.

By using these normalized thrust and torque coefficients, three types of graphs are plotted (see Figures 3.2, 3.3, 3.4). The graphs at left side show the results of the measurements performed at $M_{tip} = 0.3$ and right side belongs to the results of $M_{tip} = 0.4$. Each measurement for each blade is consisted of five data points which represent different pitch angles (5.8°, 12°, 16°, 18° and 20°). Since for the constant RPM, thrust (C_T) or blade loading (C_T/σ) is increasing with increasing pitch angle, the direction of increasing pitch angle is same with the direction of increasing blade loading. Arrows showing the directions can be seen in figures. Moreover, since in hovering flight $C_P = C_Q$, power can be used in terms of torque in the discussion of the results. Figure 3.2 represents C_T/σ vs. C_Q/σ which is the most fundamental graph to interpret aerodynamic characteristics of any kind of aircraft. In Figure 3.3, thrust per power required (C_T/C_Q) is plotted with increasing blade loading (C_T/σ) for more convenient interpretation on aerodynamic performance of the rotor. Finally, Figure 3.4 states the blade loading vs. figure of merit (FOM) which is the efficiency parameter of helicopters.

As it can be seen in the Figure 3.2, at $M_{tip} = 0.3$ tip modifications yield a smaller C_Q/σ values compared to the rectangular blade while having almost the same blade loadings (C_T/σ) with the rectangular blade. After 16° pitch angle, at higher blade loadings, a drop in the thrust is observed in the TSA configuration. At $M_{tip} = 0.4$, it is seen that data points come closer to the rectangular blade in y direction. In other words, the torque efficiencies of the tip modifications decrease. Similarly, the TAPER and the TSA configurations have lower thrust values after 16° pitch angle.

For more convenient interpretation on the aerodynamic performance, thrust per power required is plotted for changing blade loadings (see Figure 3.3) therefore, C_T/C_Q is used in terms of "aerodynamic performance" in the discussion of that figure. All tip modifications have a contribution on the aerodynamic performance at $M_{tip} = 0.3$.

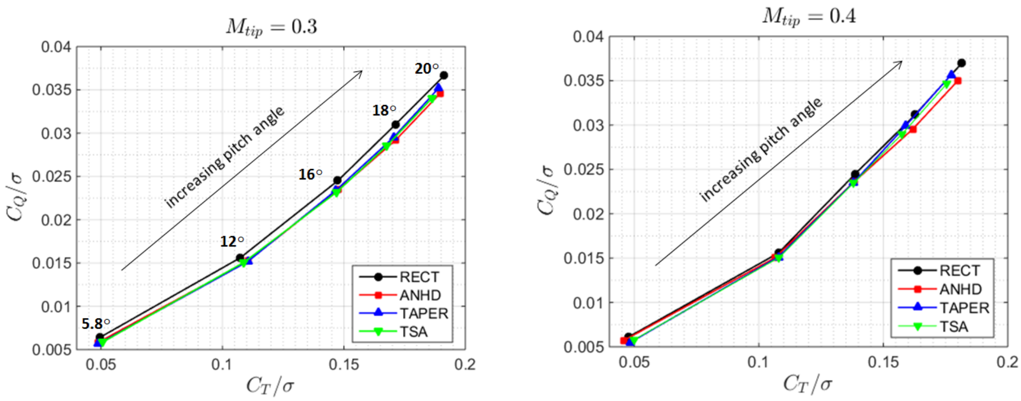

Figure 3.2: C_T/σ vs. C_Q/σ at $M_{tip} = 0.3$ (left) and $M_{tip} = 0.4$ (right)

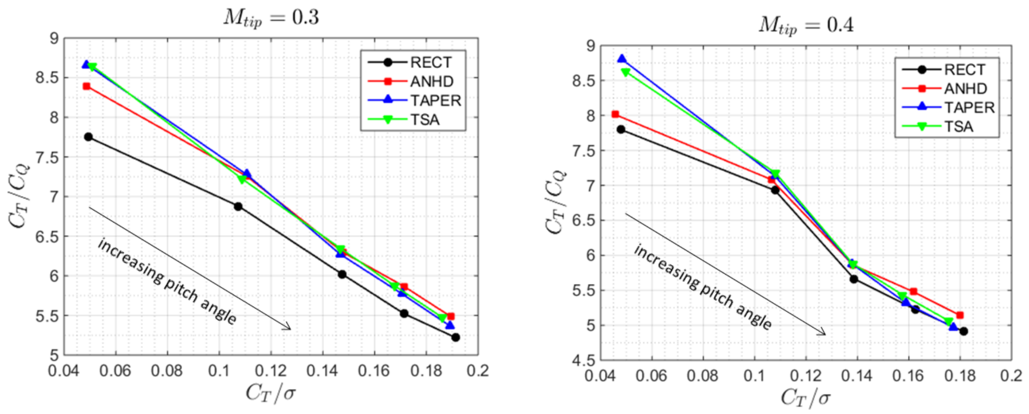

Figure 3.3: C_T/σ vs. C_T/C_Q at $M_{tip} = 0.3$ (left) and $M_{tip} = 0.4$ (right)

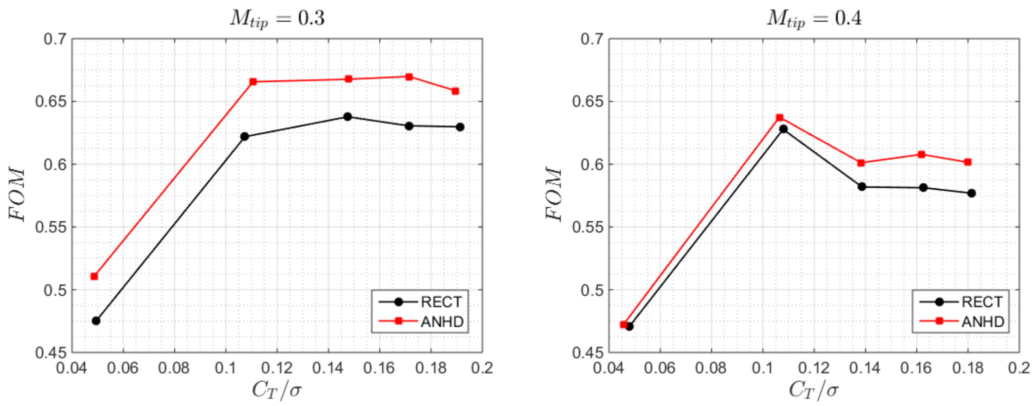

Figure 3.4: C_T/σ vs. FOM at $M_{tip} = 0.3$ (left) and $M_{tip} = 0.4$ (right)

However, at $M_{tip} = 0.4$, the TAPER and the TSA configurations show almost no improvement at high blade loadings. The reason of the reduction in thrust and the aerodynamic performance after 16° pitch angle may be explained by the premature flow separation which occurs due to the smaller chord Reynolds number together with the high angle of attack. This phenomenon was also observed in the comparison of model YUH-61A rotor and its counterpart having a tapered tip [4] (see Figure 3.5). It was revealed that the very low Reynolds number of the tapered tip can cause premature separation that does not occur at full scale. So that, although the TAPER and the TSA blades result in significant aerodynamic performance gain at low blade loadings, at high blade loadings the ANHD yields best aerodynamic performance values.

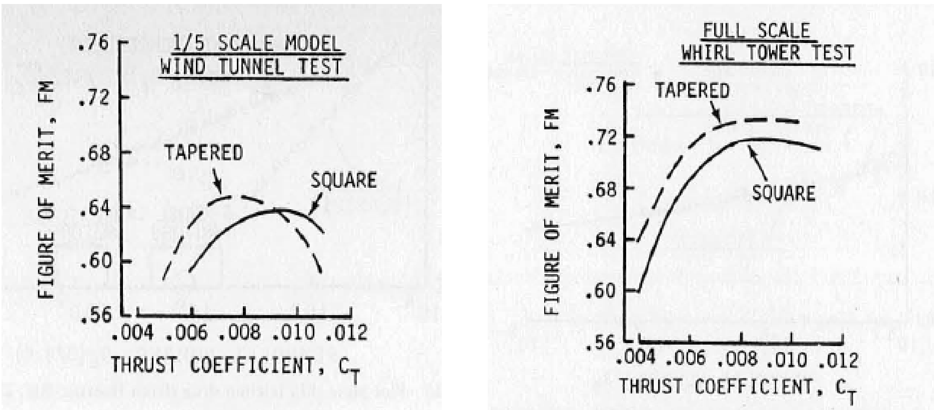

Figure 3.5: YUH-61A $1/5$ model (left) and full-scale tapered tip blade (right) hover performance [4]

Figure of merit, FOM, can be used to universally compare the aerodynamic performance of rotors that have the same blade loadings. Therefore, it is calculated and plotted for the RECT and ANHD blades which have the same blade loadings for the considered pitch angle values. (Figure 3.4). A typical FOM graph was obtained at $M_{tip} = 0.3$. As it can be seen from that graph, the ANHD improves the FOM of the reference blade by nearly 0.03 and reaches a maximum FOM value of 0.67. These values are smaller than actual helicopter FOM values. This is expected since the actual operational Reynolds numbers can not be matched with the model rotors. Moreover, most of the helicopter has twist distribution on the blades which increases FOM. There are two differences between the FOM graphs at $M_{tip} = 0.3$ and $M_{tip} = 0.4$.

Firstly, there is an abrupt loss in the FOM values after 12° pitch angle at $M_{tip} = 0.4$. Leishman [1] related the peak in FOM followed by either progressive or abrupt decrease thereafter to the airfoil shape and stall characteristics [1]. Secondly, it is seen that the FOM values at $M_{tip} = 0.4$ are smaller than in the case of $M_{tip} = 0.3$ for almost all pitch and blade configurations. That general aerodynamic performance loss again can be related to the airfoil characteristics. As discussed in the Section 1.1, helicopter airfoil is designed for a specific range that gives the maximum lift to drag ratio, higher drag divergence Mach number, maximum lift coefficient and the lowest pitching moment. It can be inferred from Figure 3.6 that VR-7 is designed to give the maximum lift coefficient at Mach numbers about 0.5. In the region between Mach numbers of 0.3 and 0.4, the maximum lift coefficient displays a decreasing trend. In order to investigate the underlying reason behind this performance decrease and verify the relation with the inherent characteristics of the VR7 airfoil, thrust and torque variations for all the tested blades are plotted for tested Mach numbers in Figure 3.7. It was found that the loss in the aerodynamic performance at $M_{tip} = 0.4$ mainly due to the decrease in the thrust coefficient which agrees with the airfoil characteristics (Figure 3.7).

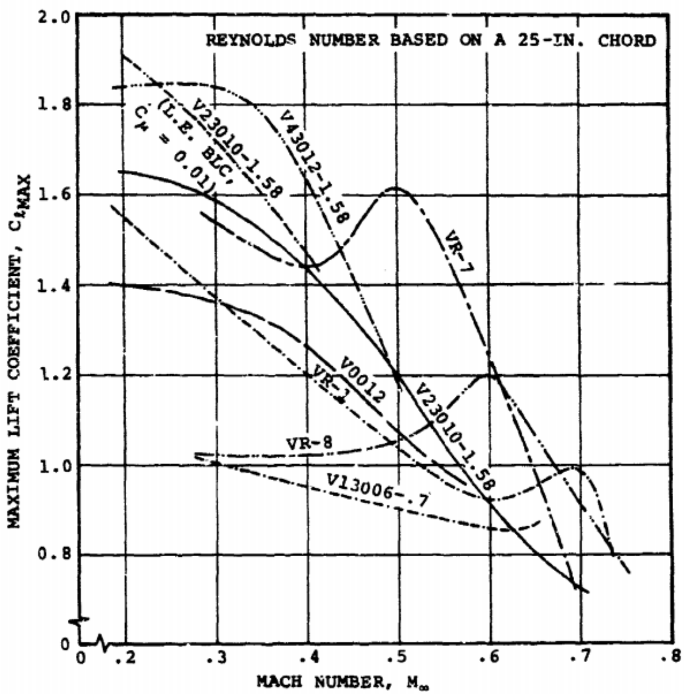

Figure 3.6: Mach number vs. Cl_{max} for various airfoils including VR-7 [5]

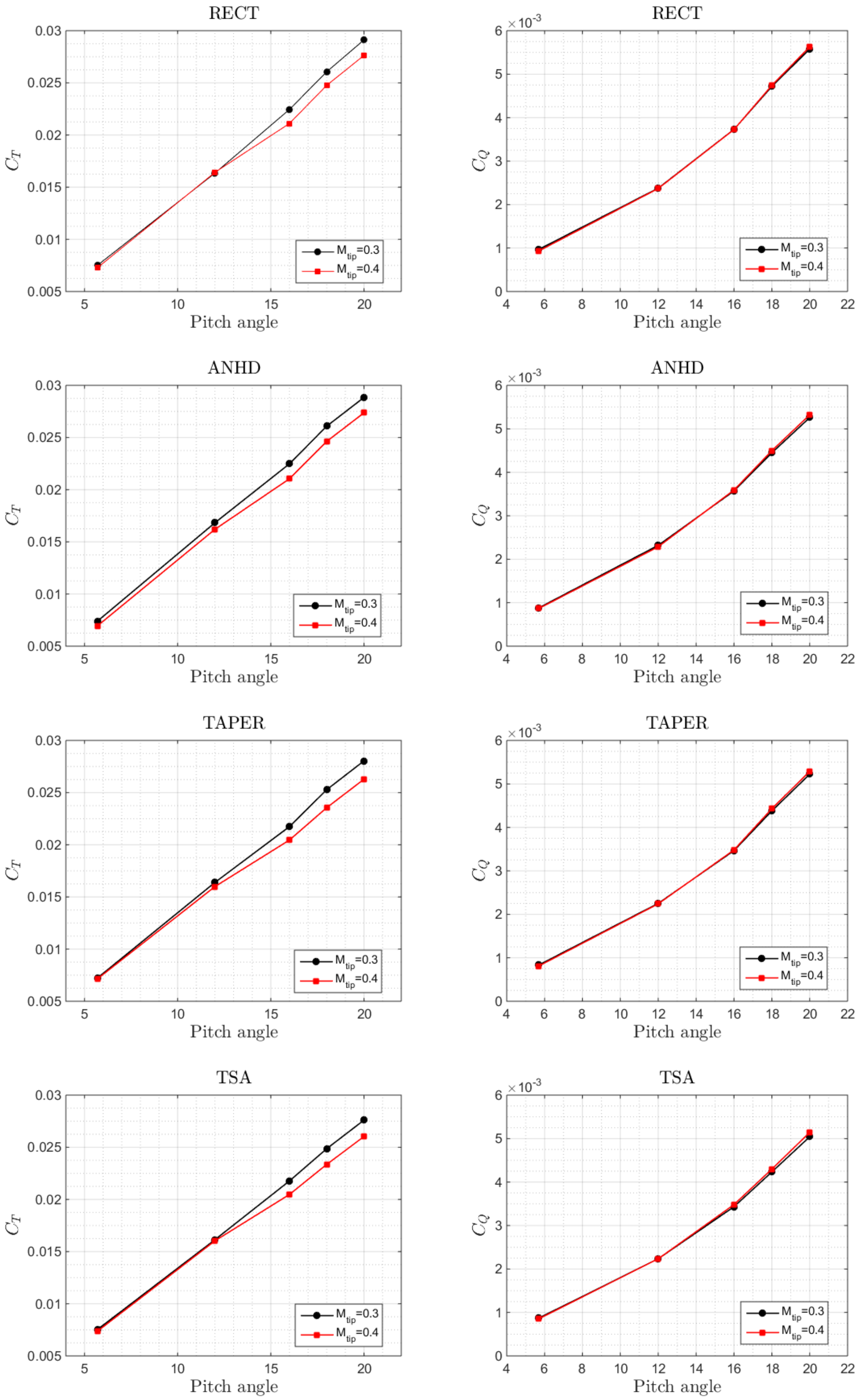

Figure 3.7: Effect of the Mach number on C_T and C_Q (for all blades)

3.2 Vortex Characteristics

Contours of out-of plane vorticity superimposed by ensemble-averaged velocity vectors are plotted for the RECT blade for all of the captured phase angles (in Figure 3.8). As mentioned before, in the measurement plane three vortices that are shed from the three subsequent blades can be captured. When the tip vortex starts to form at the tip of the first blade ($\phi = 0°$), there are two vortices ($\phi = 72°$ and $\phi = 144°$) in the field of view which were generated by the preceding two blades. Due to the symmetry of the flow in hover condition, the wake can be considered as the timeline of a tip vortex shed from any of the blades. Therefore, vortex characteristics can be investigated up to 150° phase angle; in other words, up to the location where the third vortex goes out from the measurement plane.

As the blade rotates, the newly formed tip vortex moves radially toward the root of the rotor while it convects downstream. This radially directed motion is more dominant in the immediate wake of the blades, whereas the tip vortices in the relatively far wake convect more in the horizontal direction.

The vortex diffusion with increasing wake age is consistent with the reduction in the amount of maximum vorticity contours as the vortex progresses in the wake. The shapes of the vorticity contours are becoming elliptic after the phase angle of 24°, which may be attributed to the angle between the measurement plane and the vortex tube as well as the influence of the meandering on the ensemble averaging process. Another observation is that the maximum vorticity contour which corresponds to the vortex core does not match exactly with the position of zero velocity vectors especially for the second and the third vortex (at later wake ages). This is most likely due to meandering motion on the averaging process.

To find the vortex-induced velocities, vortex core convection velocities in axial and radial directions should be subtracted from the measured velocity vectors. As it mentioned previously, dominant convection direction changes with the wake age. Moreover, it is known from the Langrebe's vortex trajectory formulas [7], that the trajectory of the vortex changes after first blade passage which is 72° for this case.

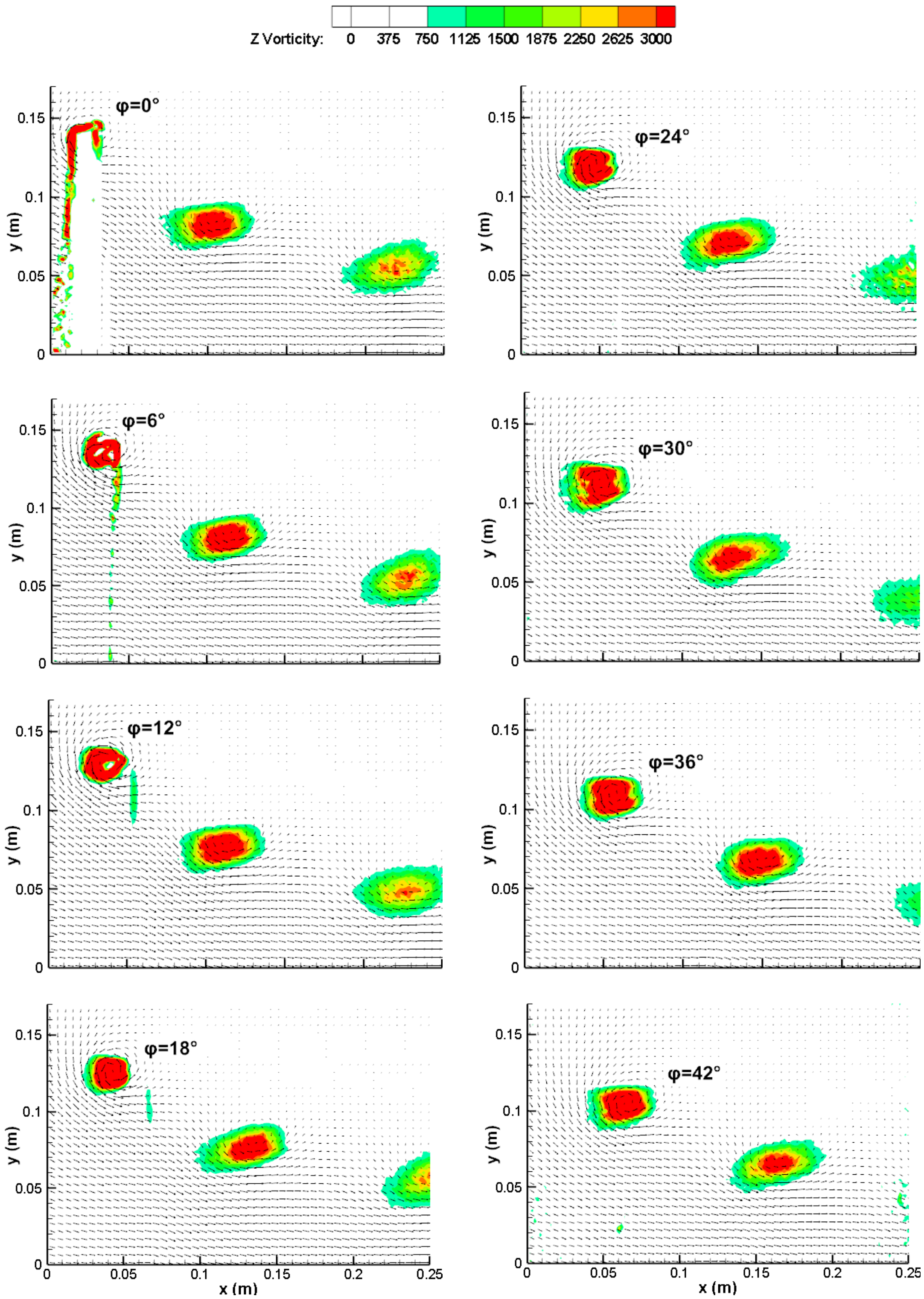
Z Vorticity: 0 375 750 1125 1500 1875 2250 2625 3000
φ=0°
φ=6°
φ=12°
φ=18°
φ=24°
φ=30°
φ=36°
φ=42°
y (m)
x (m)
0 0.05 0.1 0.15
0 0.05 0.1 0.15 0.2 0.25

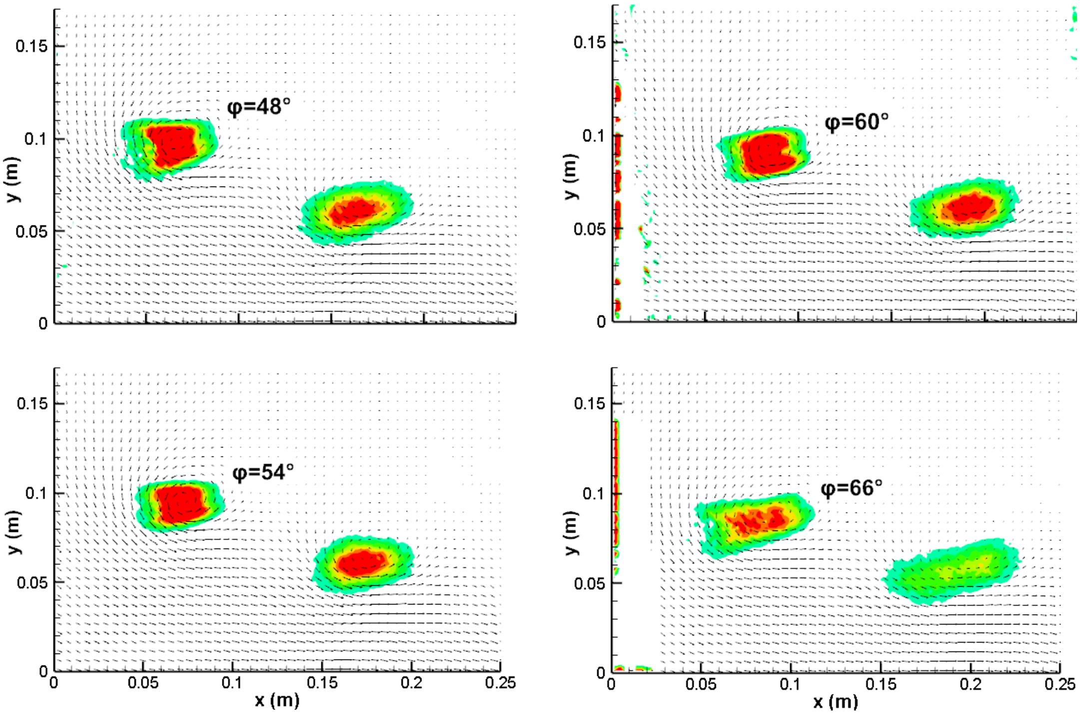

Figure 3.8: Ensemble-averaged contours of out-of-plane vorticity for RECT blade

Therefore, the convection velocities are assumed to be constant in the phases between 0°-72° and 72°-144° and they are calculated for these stages separately by dividing the distance between the center of vortices (e.g. at $\phi = 0°$ and $\phi = 72°$) to the time between the two phases. Centroids of the vortices were identified by using the maximum vorticity method in which the point with maximum ensemble averaged vorticity is defined as the centroid of the vortex.

Many methods are developed to detect vortex center such as centroid of Q (CoQ), centroid of vorticity, normalized-helicity, γ_1 integral method [32]. These methods identify coherent structures by an instantaneous local swirling motion in the velocity field, which are indicated by closed or spiral streamlines or pathlines in a suitable reference frame. In this study, the center of the tip vortex is tracked by use of the γ_1 scheme. γ_1 method initially defines a scalar function γ_1 by using the topology of the velocity field and determines the vortex center according to the local maximum point of the γ_1 [52]. As this algorithm is not Galilean invariant, the calculations were performed after subtracting the convection velocity of the particular vortex of interest at each measurement phase. A conditional averaging, which is the suggested method for rotor tip vortex studies, is then applied on the vector field in a limited neighbourhood of the vortex in order to eliminate the effects of vortex meandering and to improve signal-to-noise ratio. The conditionally averaged vortex centers at each phase angle are used to display vortex trajectory for all blades. Moreover, the conditional-averaged velocity vector fields are used for further analysis of the tip vortex behaviour, such as vorticity, vortex tangential velocity profile or circulation.

The radial and axial coordinates of the vortex were presented as non-dimensional parameters and curve fitted by two term exponential function (Figure 3.9). Definition of the exponential function and constants can be seen in Equation 3.10 and Table 3.1. There is an abrupt change in the trajectories of all of the blades after the first blade passage ($\phi = 72°$, it corresponds to 10. data point for each blade or $x/c \approx 1$ for the RECT blade). Moreover, it can be seen from the figure that the tip vortex in the cases of the ANHD, the TSA and the TAPER convect more radially than that in the case of the rectangular blade. On the contrary, axial convection rate can be ordered high to low as RECT>ANHD>TAPER>TSA which is probably due to amount of the induced velocity. Because lower induced velocity decreases the downwash behind the blade. From the general view of the trajectories, it can be said that the wake contraction ratio is higher in the modified blades which agrees with the lower torque values (see Appendix A) and it may be related to the vortex induced velocities.

The overall average of 12 phases for the ensemble averaged vorticity and axial velocity are plotted and superimposed with the conditional averaged vortex centers (Figure 3.10). The area which is affected by the presence and the reflections of the blade is covered with a gray rectangular shape. The white line represents the location of the laser sheet which cuts the quarter chord of the tested blade and the tip of that line is assumed as the location of vortex formation. It is observed that vortex trajectory follows the maximum vorticity contours. Moreover, the decreased level of vorticity for the modified blades can be noticed. The wake streamline which is consistent with the vortex trajectory can be seen from the axial velocity plots. It can be inferred from the graph that the axial velocity is lower near the blade tip for the modified blades when compared to the RECT blade which may be related to the vortex induced velocities.

Table 3.1: Functions of the exponential fitting models

	a	b	c	d
RECT	-0.6814	0.1825	1.175	-2.581
ANHD	1.117	-1.622	-1.031	0.03596
TAPER	-0.8781	0.1365	0.9817	-2.3
TSA	-0.9287	0.1237	0.7957	-2.402

$$f(x) = ae^{bx} + ce^{dx} \tag{3.10}$$

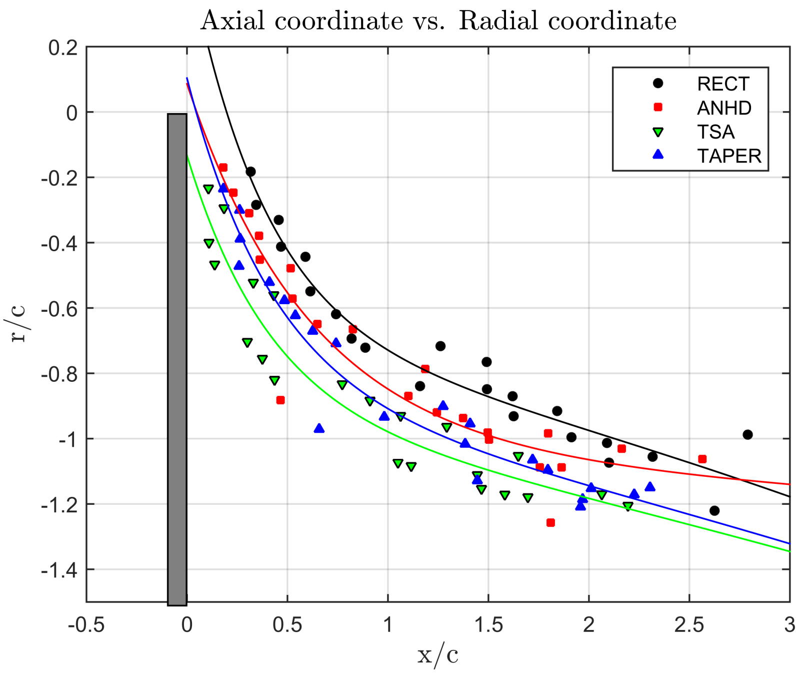

Figure 3.9: Vortex trajectory for all geometries

In order to assess the effect of meandering, contours of conditional averaged out-of-plane vorticity are plotted for the $\phi = 42°$ for all blade tip configurations (Figure 3.11). As expected, the vortices show circular behaviour and zero velocity vectors coincide with the vortex cores when the meandering effect is eliminated. It is also evident from the vorticity plots that in the case of the TAPER and the TSA configurations, the vorticity levels of the tip vortices decrease considerably (44% reduction in vorticity compared to the RECT blade).

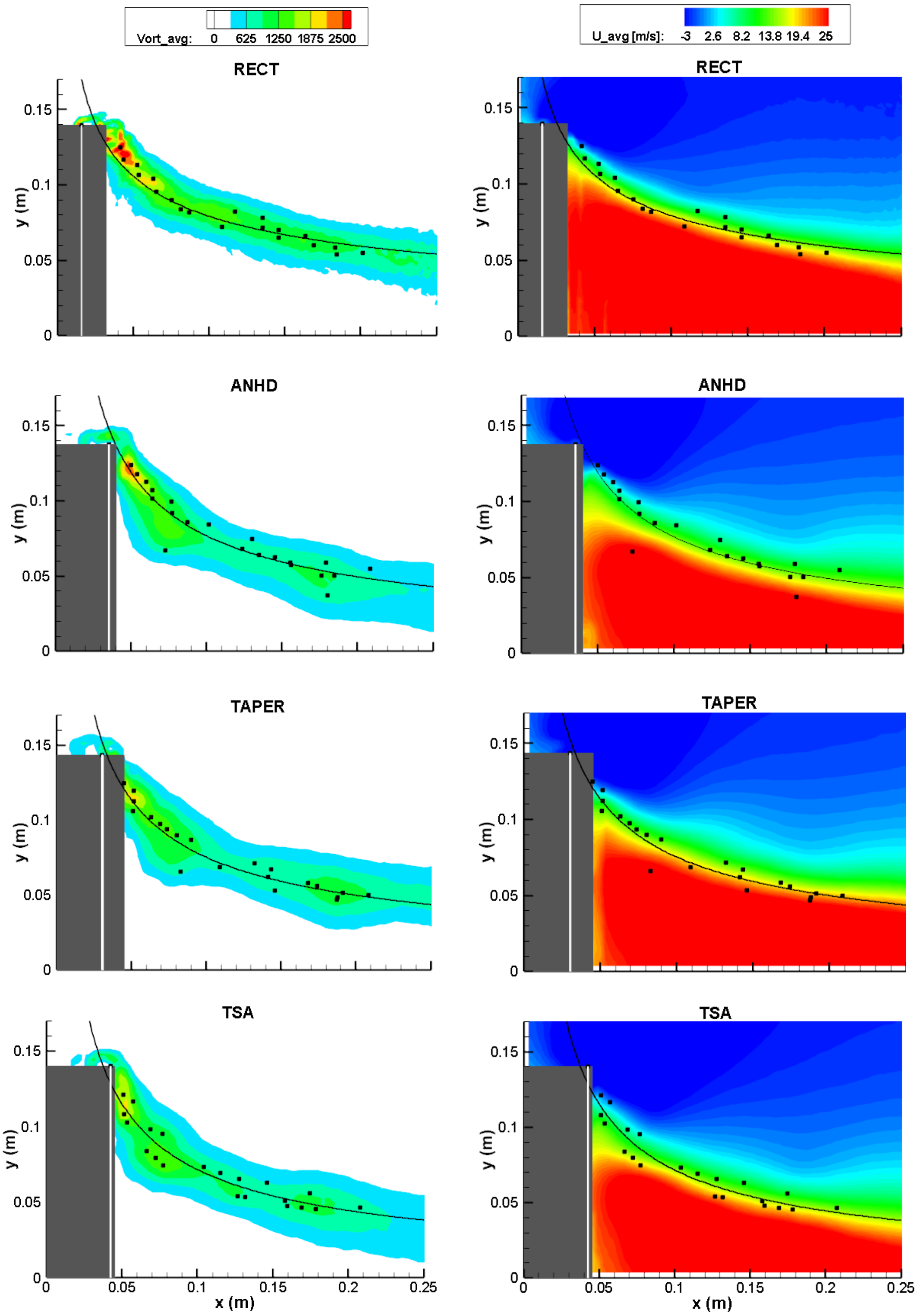

Figure 3.10: The overall average of 12 phases (0° to 72° with 6° intervals) for ensemble averaged vorticity (left) and ensemble averaged axial velocity (right) of each phase for all blades

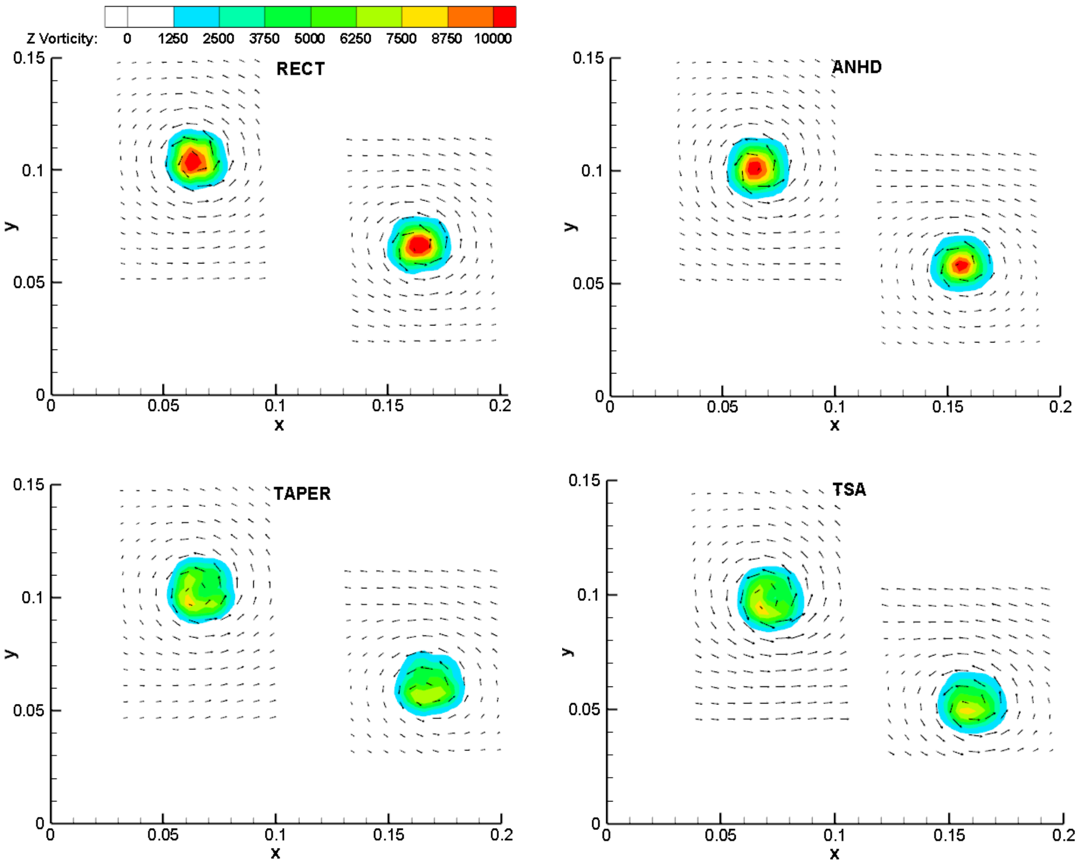

Figure 3.11: Conditional averaged contours of out-of plane vorticity for $\phi = 42°$

Velocity profiles along a horizontal axis passing through the centers of the tip vortices are obtained from the conditional-averaged velocity fields for the phase range of 18° - 150° for all blades. Velocity profiles of the vortices at early wake ages can not be captured due to the poor image quality caused by the presence of the blade in the field of view. Vortex velocity profiles at the phases of $\phi = 42°$ and $\phi = 114°$ are presented in Figure 3.12. In spite of fewer data points close to center due to the poor seeding, the velocity profiles are almost symmetrical and velocity is very close to zero at the center (at r/c=0). Decreasing maximum tangential velocity with increasing wake age can be observed by comparing the two plots. However, there is no noticeable core radius change between two phase angles. In terms of the effect of tip geometries on velocity profiles, it can be deduced that the ANHD reduces the maximum tangential velocity by 20%; the TAPER and the TSA reduces it by 30%. An increase in vortex radius can also be observed for the TAPER and the TSA.

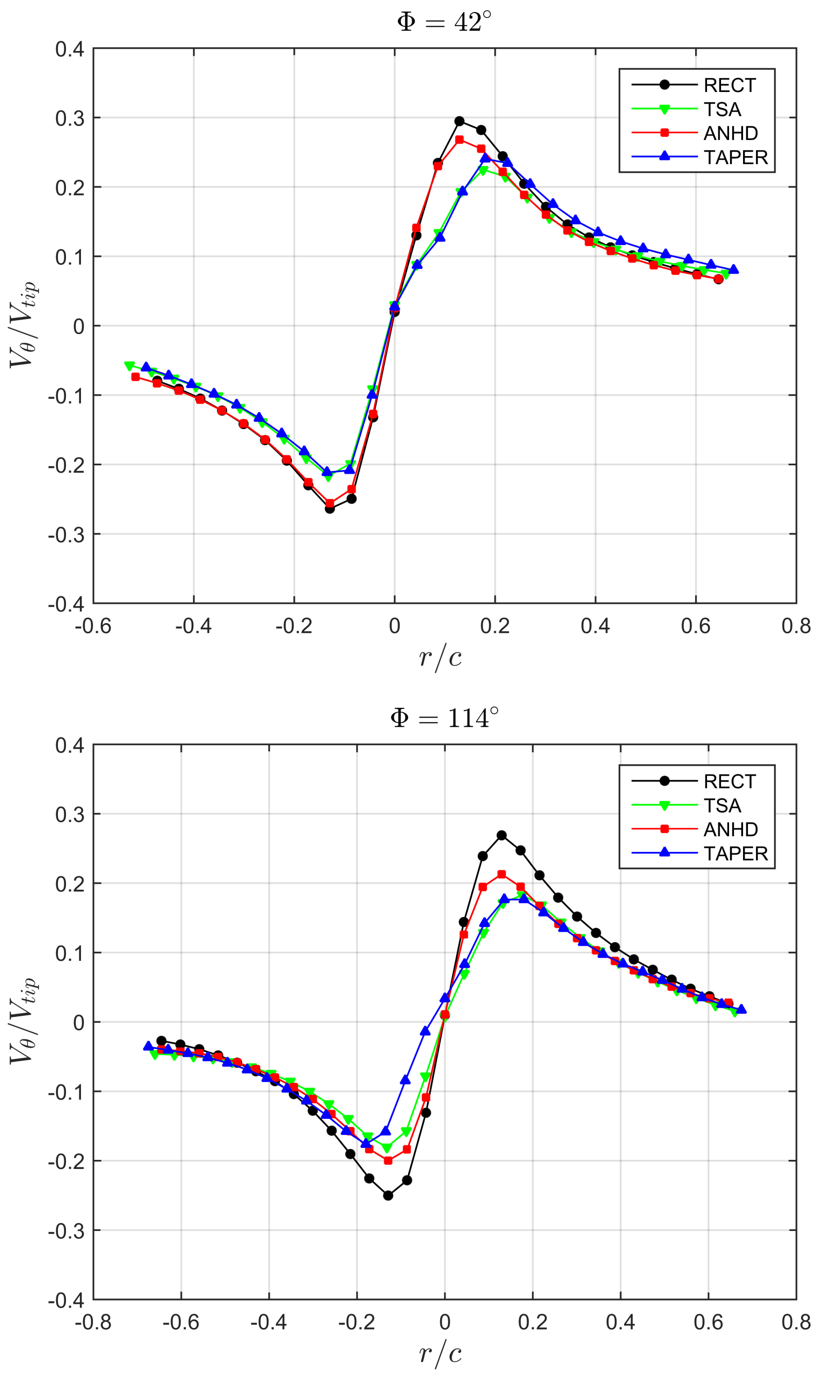

Figure 3.12: Tangential velocity profiles at $\phi = 42°$ and $\phi = 114°$

The magnitude of the peak tangential velocity of the tip vortex is an important parameter in terms of vortex sound generation during BVI [15]. In this context, phase-history of the maximum tangential velocities of the tip vortices are plotted in Figure 3.13, which is complemented with a curve fitted by use of a linear regression. As expected, $V_{\theta,max}$ is decreasing with wake age due to the diffusion of the tip vortex.

The highest velocity occurs in the case of the RECT blade. It is obvious that all of the tip modifications result in a decrease in the magnitude of the peak tangential velocity and the minimum $V_{\theta,max}$ is achieved in the case of the TSA blade. The order of blades in terms of vortices having the maximum tangential velocity agrees with the order of axial convection velocity rate and measured torque which are parameters related to induced velocity.

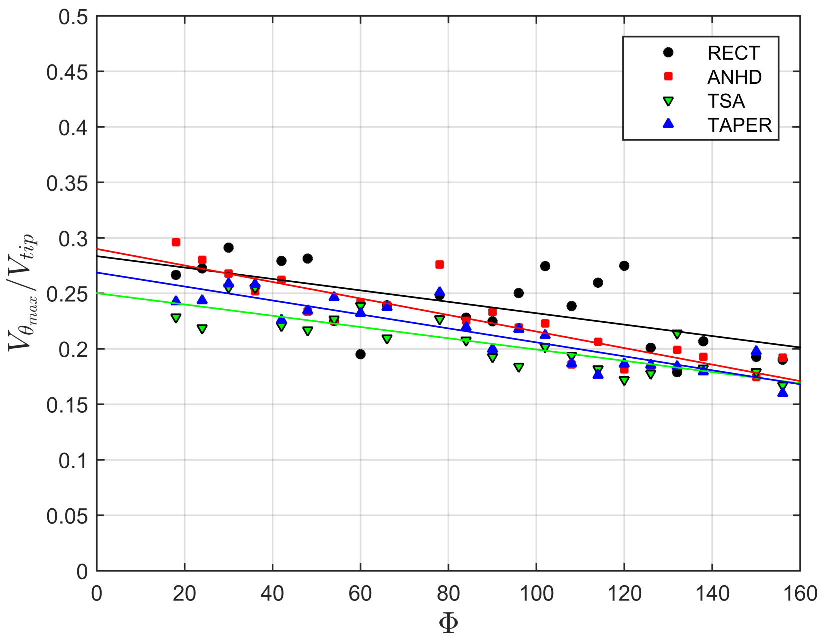

Figure 3.13: Maximum tangential velocities vs. Wake age

Figure 3.14 shows the dimensionless circulation of the tip vortex with a linear curve fit. Similarly, circulation values decrease as the vortex convects downstream in the wake of the blades. Although the TAPER and the TSA have the minimum vorticity and tangential velocities, the ANHD blade has the minimum circulation level with a 13% reduction in circulation compared to the RECT blade which probably originates from the difference in vortex core diameters. Because the total circulation of a vortex is defined as the integral of the vorticity over a surface that encompasses the limits of the flow field [16]. Moreover, it is formulated as $\Gamma(\bar{r}) = V_\theta(\bar{r})2\pi r_c$ in vortex models and used to represent vortex strength [1]. In other words, although the vorticity and the velocity of the tip vortex is lower in the case of the TAPER and the TSA, the enclosed area -vortex core size- is higher. That results in higher circulation values compared to the ANHD blade. So, once again vortex circulation or strentgh is the minimum in the case of the ANHD blade which is in accordance with the aerodynamic performance results. The mechanism behind the ANHD blade in terms of increased performance was explained in the study of Fitzgibbon etc. [41] by reduced loading at the tip region of the blade.

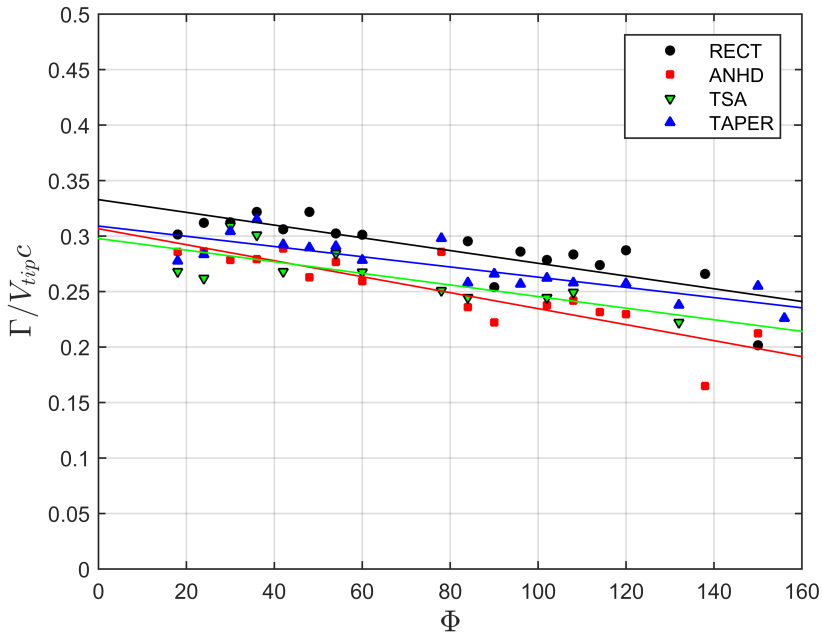

Figure 3.14: Tip vortex circulation vs. Wake age

As mentioned before, conditional averaging is applied on 100 vector fields. Figure 3.15 shows 100 vortex centroids together with the conditional averaged center (yellow dot with black marker line) for a selection of phases and for all the blade geometries. The amount of wander, as expected, increases with the increasing vortex age for all geometries. Moreover, the wandering motion rotates with increasing vortex age in a clockwise direction. The average standard deviation of the center locations for all blades are found nearly 0.15c in the axial direction and 0.1c in the radial direction. That higher axial aperiodicity of the vortices can easily be noticed from the graphs. It is also observed that in the ANHD and TSA configurations, the wandering amplitude is greater than the other two cases.

Vatistas [53] developed a formula for tangential velocity of laminar vortices. Where Γ is circulation, r_c is core radius, $\bar{r} = r/r_c$ is non-dimensional radial coordinate and n is an integer. Depending on the value of parameter n, some of the traditional vortices

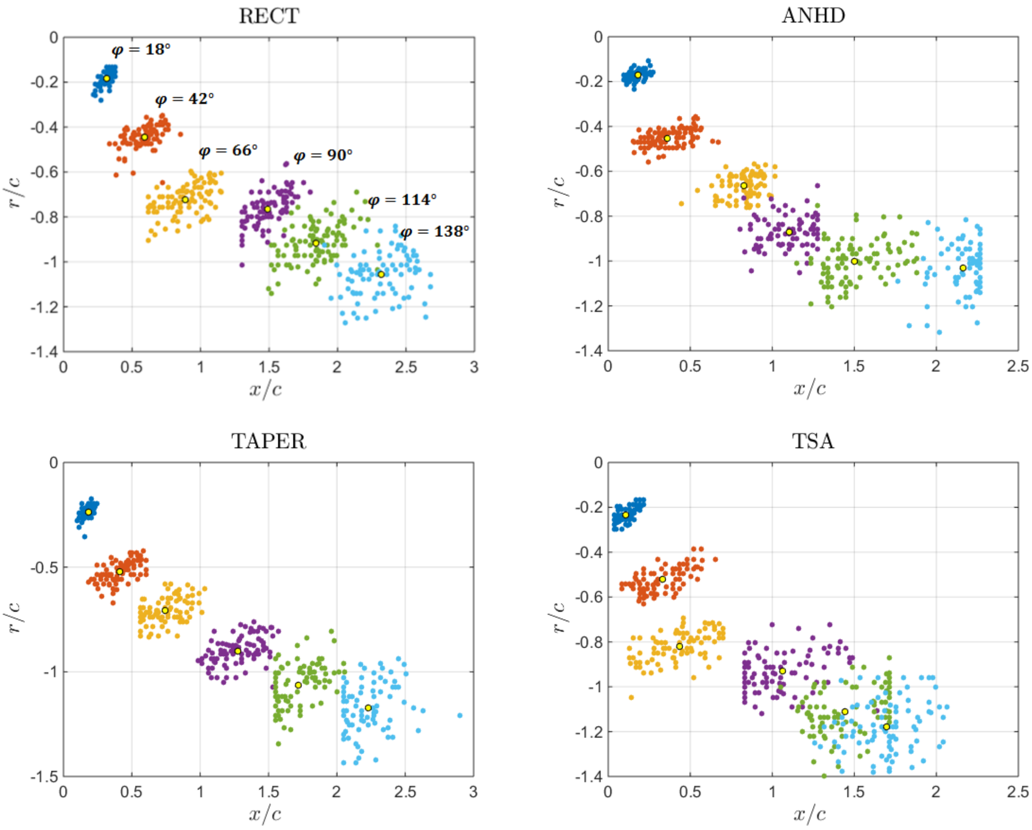

Figure 3.15: Scatter plots for $\phi = 18°$-$\phi = 138°$

like Rankine's ($n \to \infty$), Kaufmann's, and Scully's ($n = 1$) could be retrieved. It was found that $n = 2$ which is also a good approximation of Lamb-Oseen vortex model gives best fit with the many experimental data [1].

$$V_\theta(\bar{r}) = \frac{\Gamma}{2\pi r_c} \frac{\bar{r}}{(1 + \bar{r}^{2n})^{1/n}} \tag{3.11}$$

By using the calculated circulation and core radius values, vortex models are compared to the measured tangential velocity profiles for the different blades at the chosen phase angle of 42°. There is a good agreement between the models (Vatistas $n = 2$ and Lamb-Oseen) and the vortices of the RECT and ANHD blades. Small disunities may result from asymmetric velocity profile and core radius or fewer data points. However, for the case of TAPER and TSA, shape of the models do not fit well with the data. More diffused vortex structure besides the previous factors may cause that divergence between the experimental velocity data and the models.

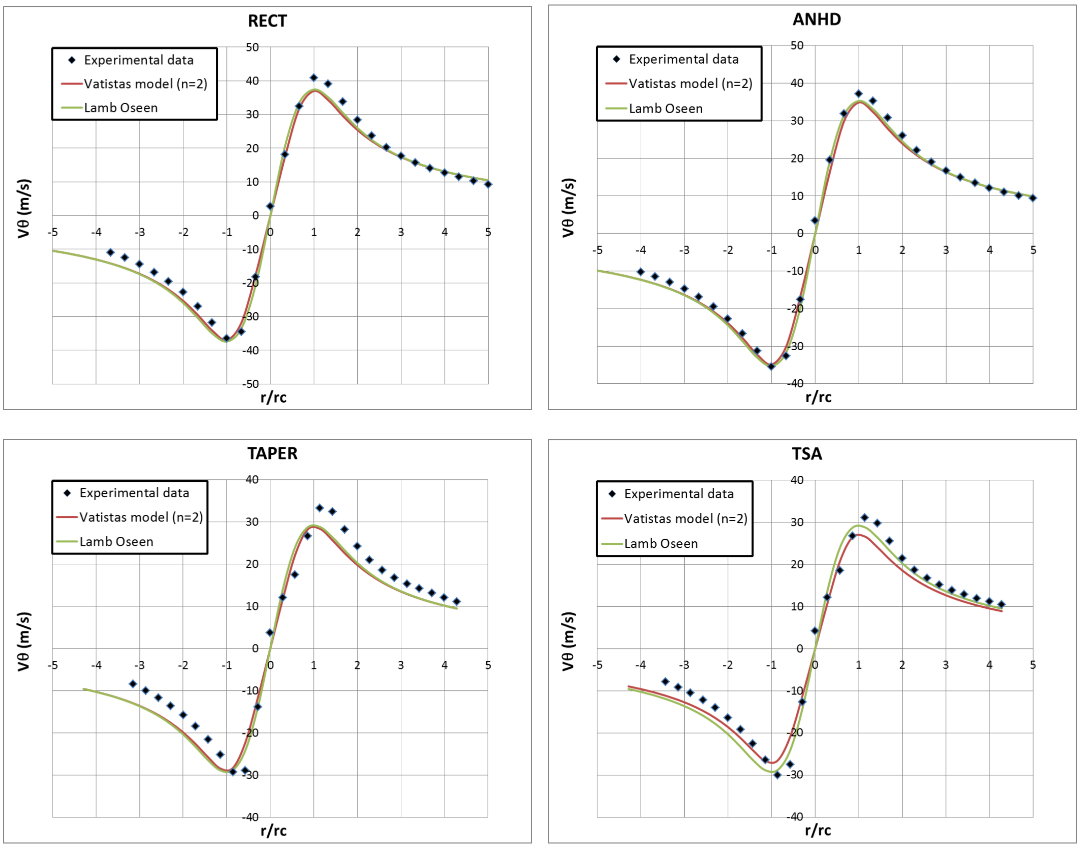

Figure 3.16: Comparison of vortex models with measured tangential velocity data at $\phi = 42°$

CHAPTER 4

CONCLUSION

The objective of this study is to experimentally investigate the effects of helicopter blade tip geometries on rotor aerodynamic performance and tip vortex characteristics in hovering flight. Therefore, load (thrust and torque) and flow field measurements were performed on a model rotor test setup with four different blade tip configurations, i.e., rectangular (RECT), anhedral (ANHD), tapered (TAPER) and taper-swept-anhedral (TSA). Thrust and torque data were captured by using a loadcell and torque meter. The measurements were performed at five different pitch angles (5.8°, 12°, 16° 18°, and 20°) and two different tip Mach numbers (0.3 and 0.4). The data were used to calculate thrust and torque coefficients and figure of merit (FOM) which is an indicator of rotor performance.

It was found that all tip modifications have a positive effect on the aerodynamic performance when compared to the rectangular tip configuration. This improvement is prominent especially at low blade loadings. Despite the lower C_Q/σ produced by the TAPER and the TSA configurations, they also lose thrust (C_T/σ) which results in lower FOM values. Overall, the ANHD tip configuration gives the best performance at high blade loadings and reaches a maximum FOM value of 0.67 and provides a FOM improvement of approximately 0.03 compared to the RECT blade at $M_{tip} = 0.3$.

Phase-locked PIV measurements were conducted at 6° intervals between 0° -72° phase angles at the selected pitch angle of 16° and tip Mach number of 0.4 for all blades. From the conditional-averaged velocity vectors, the characteristics of the tip vortex like its coordinates, tangential velocity profile and circulation were calculated.

Typical behaviour of the tip vortex with increasing wake age is examined for all tip geometries. As the blade rotates, the newly formed tip vortex moves radially toward the root of the rotor while it convects downstream. This downward directed motion is more dominant in the immediate wake of the blades, whereas the tip vortices in the relatively far wake convect more in the horizontal direction. The decrease in peak tangential velocity and increase in meandering motion for all blades agrees with diffusion of the vortex as it propagates within the flow.

When the effect of different blades on vortex characteristics are compared, it is observed that tip modifications change the vortex trajectory, reduce the tangential velocity, and decrease the circulation levels of the tip vortex. The tip vortex in the cases of the ANHD, the TSA and the TAPER blades convect more radially than that in the case of the RECT blade. On the contrary, the tip vortex in the case of the RECT blade has a higher axial convection. The TAPER and the TSA configurations have the minimum peak tangential velocities but have higher vortex core diameters. The minimum tip-vortex circulation level, which can be used as an indicator of vortex strength, is achieved in the case of the ANHD blade, which is in agreement with the highest FOM obtained with this blade. The scatter of the vortex centroids, which is due to the meandering motion, is higher in the configurations of the ANHD and the TSA. Vatistas $n = 2$ and Lamb-Oseen models match well with the vortices of the ANHD and the RECT blade, however the vortices in the case of the TAPER and the TSA blades does not fit exactly with any of the model probably due to the more diffused structure of the vortices.

For future works, some suggestions are listed below.

- With this experimental setup, a maximum tip Mach number of 0.4 was reached. It is important to get the tip Mach similarity with full scale rotors, which is nearly 0.6 in hover, for accurate performance estimation since Mach number has a significant effect on the airfoil characteristics.
- It is stated that the TAPER and the TSA configurations may be exposed to flow separation at high blade loadings due to lower chord Reynolds number of the model rotor. If this is the case, the TSA can be the optimum tip shape in hover for the full-scale case by using the advantages of the anhedral angle and the

tapered tip without stall. Therefore, it is suggested to perform a full-scale rotor test to see whether the performance of tapered blades is decreasing or not at higher blade loadings.

- The vortex characteristics were investigated up to $150°$ phase angle; moreover, due to the shadow of the blade and reflection of the laser, the vortices close to the blade at early wake ages can not be detected. Therefore, measurement area can be enlarged by using two measurements planes and it can be performed detail measurements focusing on the early wake ages by arranging the sheet and blade positions which make shadow and reflections minimum.

- Lower data points near vortex core due to poor seeding can be minimized and more accurate vortex parameters can be obtained by using new technology particles like Helium-filled soap bubbles [54].

- Aerodynamic performance results and the vortex characteristics can be compared to numerical analysis of the rotor test setup. Moreover laser sheet can be placed perpendicular to vortex tube for every phase angle with the apriori of vortex tube angle which is calculated numerically.

- Finally, it is suggested to perform experiments at different flight conditions for future work with a modified experimental setup in a wind tunnel which will allow for forward flight simulation.

REFERENCES

[1] J. G. Leishman. *Principles of Helicopter Aerodynamics*. Cambridge University Press, second edition, 2006.

[2] A. Brocklehurst and G. N. Barakos. A Review of Helicopter Rotor Blade Tip Shapes. *Progress in Aerospace Sciences*, 56:35–74, 2013.

[3] P. Marques, A. Maligno, S. Dierks, V. Penev, and A. Bachouche. The Jinn Military Unmanned Helicopter Program : Rotor Blade Tip Aerodynamics of the Advanced Technology Demonstrator. *International Journal of Unmanned Systems Engineering (IJUSEng)*, 1(3):6–15, 2013.

[4] C. N. Keys, M. A. Mcveigh, and F. J. Mchugh. Estimation of Full-Scale Rotor Performance from Model Rotor Test Data. *Journal of the American Helicopter Society*, 30(4):22–29, 1985.

[5] L. U. Dadone. U.S Army Helicopter Design Datcom Volume I-Airfoils. Technical Report ADA-033425, U.S. Army, 1976.

[6] W. Johnson. *Rotorcraft Aeromechanics*. Cambridge University Press, 2013.

[7] A. J. Landgrebe. The Wake Geometry of a Hovering Helicopter Rotor and Its Influence on Rotor Performance. In *28th Annual National Forum of the American Helicopter Society*, May 1972.

[8] J. L. Tangler, R. M. Wohlfeld, and S. J. Miley. An Experimental Investigation of Vortex Stability, Tip Shapes, Compressibility, and Noise for Hovering Model Rotors. Technical Report CR-2305, NASA, September 1973.

[9] J. L. Tangler. Experimental Investigation of the Subwing Tip and Its Vortex Structure. Technical Report CR-3058, NASA, November 1978.

[10] C. Tung and F. X. Caradonna. Experimental and Analytical Studies of Model

Helicopter Rotor in Hover. In *6th European Rotorcraft and Powered Lift Aircraft Forum*, number 25, September 1980.

[11] U. Rerry and E. Raymond. Wind-Tunnel Test of an Articulated Helicopter Rotor Model With Several Tip Shapes. Technical Report TM-80080, NASA Technical Memorandum, 1980.

[12] W. H. Weller. Experimental Investigation of Effects of Blade Tip Geometry on Loads and Performance for an Articulated Rotor System William. Technical Report TP-1303, NASA Technical Paper, January 1979.

[13] C. Tung, Caradonna F. X. Pucci, S. L., and H. A. Morse. The Structure of Trailing Vortices Generated by Model Rotor Blades The Structure of Trailing Vortices Generated by Model Rotor Blades. Technical Report TM-81316, NASA Technical Memorandum, August 1981.

[14] T. L. Thompson, N. M. Komerath, and R. B. Grayj. Visualization and Measurement of the Tip Vortex Core of a Rotor Blade in Hover. *Journal of Aircraft*, 25(12):1113–1121, 1988.

[15] D. Smith, D. Sigl, and E. Dudley. Helicopter Rotor Tip Shapes for Reduced Blade Vortex Interaction an Experimental Investigation. The University of Oklahoma Norman , OK 33rd Aerospace Sciences Meeting and Exhibit. In *33rd Aerospace Sciences Meeting and Exhibit*, January 1995.

[16] J. G. Leishman, A. Baker, and A. Coyne. Measurements of Rotor Tip Vortices Using Three-Component Laser Doppler Velocimetry. In *AHS Aeromechanics Specialists' Conference*, Farfield Country, 1996.

[17] B. R. Mullins, D. E. Smith, C. B. Rath, and S. L. Thomas. Helicopter Rotor Tip Shapes for Reduced Blade-Vortex Interaction - An Experimental Investigration. In *34th AIAA, Aerospace Sciences Meeting and Exhibit*, January 1996.

[18] A. Iiurashige and A. Tsuchihashi. Blade-Tip Vortex Measurement by PIV. In *European Rotorcraft Forum*, pages 1–8, 1997.

[19] J. G. Leishman and A. Bagai. Challenges in Understanding the Vortex Dynamics Introduction. *AIAA Journal*, 36(7), 1998.

[20] M. Raffel and C. Willert. Vortical Flow Structures at a Helicopter Rotor Model Measured by LDV and PIV. *The Aeronautical Journal*, April 1998.

[21] M. J. Bhagwat and J. G. Leishman. Correlation of Helicopter Rotor Tip Vortex Measurements. *AIAA Journal*, 38(2):301–308, 2000.

[22] J. Heineck, M. Field, and A. J. Wadcock. Application of Three-Component PIV to a Hovering Rotor Wake. In *American Helicopter Society 56th Annual Forum*, May 2000.

[23] C. L. Burley, T. F. Brooks, N. Langley, B. Van der Wall, H. Richard, M. Raffel, P. Beaumier, and Y. Delrieux. Rotor Wake Vortex Definition - Initial Evaluation of 3-C PIV Results of the HART-II Study. In *28th European Rotorcraft Forum*, pages 1–29, September 2002.

[24] P. B. Martin, J. G. Leishman, and G. J. Pugliese. High Resolution Trailing Vortex Measurements in the Wake of a Hovering Rotor. *Journal of the American Helicopter Society*, 48(1), 2002.

[25] H. Kato, S. Watanahet, N. Kondol, and S. Saito. Application of Stereoscopic PIV to Helicopter Rotor Blade. In *20th International Congress on Instrumentation in Aerospace Simulation Facilities, ICIASF*, August 2003.

[26] Y. O. J. Han and Leishman G. Investigation of Helicopter Rotor-Blade-Tip-Vortex. *AIAA Journal*, 42(3), March 2004.

[27] B. Van der Wall and H. Richard. Analysis Methodology for 3C-PIV Data of Rotary Wing Vortices. *Experiments in Fluids*, 40:798–812, 2006.

[28] H. Richard and B. V. D. Wall. Detailed Investigation of Rotor Blade Tip Vortex in Hover Condition by 2C and 3C-PIV. In *European Rotorcraft Forum*, September 2006.

[29] M. Ramasamy and J. G. Leishman. Benchmarking Particle Image Velocimetry with Laser Doppler Velocimetry for Rotor Wake Measurements. 45(11):2622–2633, 2007.

[30] M. Ramasamy, B. Johnson, and J. G. Leishman. Turbulent Tip Vortex Measurements Using Dual-Plane Stereoscopic Particle Image Velocimetry. *AIAA Journal*, 47(8):1826–1840, 2009.

[31] K. Kindler, K. Mulleners, H. Richard, B. Van der Wall, and M. Raffel. Aperiodicity in the Near Field of Full-Scale Rotor Blade Tip Vortices. *Experiments in Fluids*, 50:1601–1610, 2011.

[32] S. M. Mula, J. H. Stephenson, C. E. Tinney, and J. Sirohi. Dynamical Characteristics of the Tip Vortex From a Four-Bladed Rotor in Hover. *Exp. Fluids*, 2013.

[33] H. Nandeesh, S. Dhwanil, R. Vrishank, P. Sorin, and K. Narayanan. Effects of Advance Ratio and Radial Location on the Vortex Structure on a Rotating Blade in Reverse Flow. In *AHS 71st Annual Forum*, 2015.

[34] A. Bauknecht, B. Ewers, O. Schneider, and M. Raffel. Blade Tip Vortex Measurements on Actively Twisted Rotor Blades. *Experiments in Fluids*, 58(5), 2017.

[35] H. Shuilin, F. Feng, Y. Mingchuan, and S. Wei. Aerodynamic Performance and Aeroacoustic Characteristics of Model Rotor with Anhedral Blade Tip in Hover. *Transactions of Nanjing University of Aeronautics and Astronautics*, 35(1):162–169, 2018.

[36] P. Rauch, M. Gervais, P. Cranga, A. Baud, F. Hirsch, A. Walter, and P. Beaumier. Blue Edge^{TM} : The Design, Development and Testing of a New Blade Concept. In *American Helicopter Society 67th Annual Forum*, Virginia Beach, VA, May 2011.

[37] A. J. Landgrebe and E. D. Bellinger. Experimental Investigation of Model Variable-geometry and Ogee Tip Rotors. Technical Report CR-2275, NASA, February 1974.

[38] P. B. Martin, M. Field, and J. G. Leishman. Trailing Vortex Measurements in the Wake of a Hovering Rotor Blade. In *58th AHS International Annual Forum*, June 2002.

[39] A. Yücekayali, M. Şenipek, and Y. Ortakaya. Main Rotor Aeroacoustic Analysis & Validation with Test Data and Favorable Planform Design for Minimal Aerodynamic Noise. In *41st European Rotorcraft Forum*, 2015.

[40] J. Lee, N. K. Sang, G. L. Sang, G. I. Dong, J. K. Hee, and J. L. Duck. Development of Improved Rotor Blade Tip Shape Using Multidisciplinary Design Analysis and Optimization. In *44th European Rotorcraft Forum*, September 2018.

[41] T. A. Fitzgibbon, G. N. Barakos, M. A. Woodgate, and A. Jimenez. Numerical Simulation of Different Rotor Designs in Hover and Forward Flight. In *44th European Rotorcraft Forum*, pages 18–21, September 2018.

[42] T. Y. Jr. William and R. M. Wayne. Wind-Tunnel Investigation of the Effects of Blade Tip Geometry on the Interaction of Torsional Loads and Performance-for an Articulated Helicopter Rotor. Technical Report TP-1926, NASA Technical Paper, December 1981.

[43] P. Kuefmann, R. Bartels, and O. Schneider. DLR ' s Multiple Swashplate Control System : Operation and Preliminary Testing . In *38th European Rotorcraft Forum*, September 2012.

[44] M. Ramasamy. Rotor Hover Performance and Flowfield Measurements with Untwisted and Highly-twisted Blades Experimental Setup Rotor System. In *36th European Rotorcraft Forum*, Paris, France, September 2010.

[45] T. Schwermer, K. Richter, and M. Raffel. Development of a Rotor Test Facility for the Investigation of Dynamic Stall Development of a Rotor Test Facility for the Investigation of Dynamic Stall. 2014.

[46] A. Yucekayali. Rotor Pallerinde Uç Girdabı Kontrolü ve Rotor Yüklerine Etkisi başlıklı DKTM projesi kapsamında, test edilecek ölçekli model için tork ve dönüş hızı gereksinim çalışması, 2016.

[47] M. Sahbaz. Rotor Test Setup CFD Simulations, 2016.

[48] B. Tasdemir. Stress Analysis of a Rotor Setup at 3000 RPM (new design), 2016.

[49] O. Cicek. Shaft Critical Speed Analysis Report, 2016.

[50] M. Raffel, C. Willert, F. Scarano, C. J. Kähler, S. T. Wereley, and J. Kompenhans. *Particle Image Velocimetry - A Practical Guide (3rd Edition)*. Springer Verlag, April 2018.

[51] C. Brossard, J. C. Monnier, P. Barricau, F. X. Vandernoot, Y. L. Sant, G. L. Besnerais, C. Brossard, J. C. Monnier, P. Barricau, F. X. Vandernoot, and Y. L. Sant. Principles and Applications of Particle Image Velocimetry . *Aerospace Lab*, 2015.

[52] L. Graftieaux, M. Michard, and G. Nathalie. Combining PIV, POD and vortex identification algorithms for the study of unsteady turbulent swirling flows. *Measurement Science and Technology*, 12(9):1422–1429, 2001.

[53] G. H. Vatistas, V. Kozel, and W. C. Mih. A Simpler Model for Concentrated Vortices. *Experiments in Fluids*, 11(1):73–76, 1991.

[54] G. Carlo, A. Caridi, A. Sciacchitano, and F. Scarano. Helium - Filled Soap Bubbles for Vortex Core Velocimetry. *Experiments in Fluids*, 58:1–12, 2017.

APPENDIX A

MEASURED THRUST AND TORQUE DATA

Mtip=0.3	RECT		ANHD		TAPER		TSA	
pitch	CT/σ	CQ/σ	CT/σ	CQ/σ	CT/σ	CQ/σ	CT/σ	CQ/σ
5.8	0.049413	0.006377	0.048664	0.005798	0.048819	0.005636	0.050854	0.005879
12	0.107407	0.015613	0.110586	0.01524	0.110539	0.015186	0.108849	0.015072
16	0.147522	0.024507	0.147718	0.023456	0.146617	0.023369	0.146843	0.023145
18	0.171257	0.031002	0.171415	0.029225	0.170507	0.029531	0.167689	0.028543
20	0.191325	0.036652	0.189515	0.034558	0.189119	0.035231	0.186168	0.034008

Mtip=0.4	RECT		ANHD		TAPER		TSA	
pitch	CT/σ	CQ/σ	CT/σ	CQ/σ	CT/σ	CQ/σ	CT/σ	CQ/σ
5.8	0.047867	0.006139	0.045682	0.005702	0.048264	0.005483	0.049759	0.005769
12	0.107886	0.015571	0.106439	0.015026	0.10785	0.015117	0.10813	0.015069
16	0.138695	0.024489	0.138289	0.023597	0.137947	0.023476	0.138094	0.023478
18	0.162721	0.03115	0.161838	0.029546	0.15888	0.029882	0.157543	0.028987
20	0.181553	0.036991	0.179833	0.034969	0.177262	0.035672	0.175572	0.03468

Table A.1: Thrust and torque coefficients per solidity for all blades and tip Mach numbers, PIV test case was colourized